A Hybrid Molecular Dynamics/Fluctuating Hydrodynamics Method for Modelling Liquids at Multiple Scales in Space and Time

Ivan Korotkin[*1], *Sergey Karabasov*[1], *Dmitry Nerukh*[2], *Anton Markesteijn*[1], *Arturs Scukins*[2], *Vladimir Farafonov*[3], *Evgen Pavlov*[2,4]

[1] The School of Engineering and Material Science, Queen Mary University of London, Mile End Road, E1 4NS, London, UK

[2] Institute of Systems Analytics, Aston University, Birmingham, B4 7ET, UK

[3] Department of Physical Chemistry, V.N. Karazin Kharkiv National University, Svobody Square 4, 61022, Kharkiv, Ukraine

[4] Faculty of Physics, Kiev National Taras Shevchenko University, Prospect Acad. Glushkova 4, Kiev 03127, Ukraine

[*] Corresponding author. E-mail address: i.korotkin@qmul.ac.uk

Abstract

A new 3D implementation of a hybrid model based on the analogy with two-phase hydrodynamics has been developed for the simulation of liquids at microscale. The idea of the method is to smoothly combine the atomistic description in the Molecular Dynamics (MD) zone with the Landau-Lifshitz Fluctuating Hydrodynamics (LL-FH) representation in the rest of the system in the framework of macroscopic conservation laws through the use of a single 'zoom-in' user-defined function s that has the meaning of a partial concentration in the two-phase analogy model. In comparison with our previous works, the implementation has been extended to full 3D simulations for a range of atomistic models in GROMACS from argon to water in equilibrium conditions with a constant or a spatially variable function s. Preliminary results of simulating the diffusion of a small peptide in water are also reported.

1. Introduction

Classical Molecular Dynamics methods are developed to such a level that they not only reproduce macroscopic (thermodynamic) and some microscopic (such as radial distribution functions, autocorrelation functions, etc) properties of simple liquids, for which they were originally designed, but also provide qualitative and sometimes quantitative description of complex bio-molecular structures and their functionality [1, 2]. Obtained atomistic details reproduce experimentally measured structural and dynamical properties of such systems from small peptides [3] to medium size proteins [4] and cell membrane [5, 6, 7] to as large as whole cellular organelles or entire viruses [8, 9]. These all-atom 'ab initio' results allow the investigation of the system at larger spatial and temporal scales providing the description at experimentally inaccessible intermediate scales between atomistic and macroscopic levels and

leading to the appearance of new kinds of objects (complicated structures of 'molecular machinery' of the cell, its sophisticated functional motions, collective dynamics of sets of molecules, etc).

Moreover, several different scales are often needed to be considered simultaneously, in a hierarchy of levels providing a holistic picture of the molecular system. Complex system of transitions from level to level, if described correctly, provides a new global understanding of the physical properties of the whole system based on the elementary low levels interactions of atoms. The importance of such description is recognized and multiscale models are developed very actively recently [10, 11, 12]. The applications cover a wide spectrum of systems in biology, chemistry, material science, and other fields [13, 14, 15, 16, 17, 18].

The development of multiscale methods for molecular systems is most often associated with the Coarse Graining (CG) idea [5, 19, 20, 21]. Here, at larger scales new objects are introduced that approximate groups of atoms as single entities. The Dissipative Particle Dynamic method is a well-known example of CG [22, 23, 24, 25], widely applied to biological objects, and implemented in popular software, such as GROMACS [26], i.e. MARTINI, and other [6, 27, 28, 29, 30]. The difficult question of correct connection between the scales is being investigated, for example, the authors of [7] describe the relationship between the MD and the CG states using a Markov process, the so-called 'cross-graining'. Another example of linking the 'fine-grained' and 'coarse-grained' phases is reported in [27, 28], where the connection is carried out smoothly through an interphase parameter λ.

One of the main disadvantages of CG methods is their strong dependence on the choice of the CG inter-particle potentials. The main goal in developing a CG method is to construct an adequate interaction potential between selected parts of the system which are considered simply

as 'larger atoms' or 'blobs' (albeit more complex than real atoms). Despite possible connections to statistical mechanics, such as between the multi-coarse-grained method and the liquid state theory [31], the CG procedure is non-trivial and strongly influences the final description of the physics of the processes in the system.

For 'simple' liquids, such as water at normal conditions, the CG procedures are well established and can be successfully used for multiscale modelling in the framework of the geometrical domain decomposition approach based on Lagrangian particle-to-particle methods. For example, in [32, 33, 34], a family of adaptive resolution methods (AdResS, H-AdresS) is proposed where an all-atom simulation was conducted in a part of the solution domain, the surrounding solvent was represented with a simplified CG description, and in the 'buffer' region in between, the atoms gradually reduced their Degrees Of Freedom (DOFs) to become CG 'blobs'. In the original work by Praprotnik et al [32], there was a special thermostat used to suppress the unphysical pressure and density rise in the hybrid buffer zone. The correction effect of this special thermostat was later replaced by the so-called free energy compensation term in the model of Español et al [34], which made the method energy conservative at the price of losing the momentum conservation.

Another class of multiscale methods is based on representing a part of the system as a structure-less continuum. In the MD community these are known as 'implicit solvent' models and they are used for economical modelling of water and other solvents surrounding the molecule of interest. Historically first attempts to link different scales in molecular systems use this idea allowing the atoms to leave and enter the continuum part of the system. A serious conceptual problem here is the existence of a boundary between the atomistic and continuum (hydrodynamic) parts. Achieving correct balance of mass and momentum flow across this

boundary without introducing artefacts in the fully atomistic part of the simulation, which is very sensitive to the interface location between the atomistic and hydrodynamic representations of the same liquid, is a very non-trivial task [35]. In the so-called state variables schemes [10, 13, 17], the coupling between the fully atomistic and hydrodynamic regions is established with particle-in-cell type of methods. In such methods, the Lagrangian (MD particles) and Eulerian (continuum) parts of the system are coupled through a finite size overlapping zone ensuring the conservation of bulk mass and momentum fluxes. The use of the overlapping zone allows for a smoother transition between the two representations in comparison with the flux coupling through a boundary interface. In the state variables schemes, there is always some interpolation 'switch' parameter used. The meaning of this parameter in the hybrid 'buffer' zone between the pure atomistic and the pure continuum parts of the domain is typically obscure.

In Markesteijn et al [12] and Pavlov et al [18], a different approach for state variable coupling between the molecular dynamics and hydrodynamics representations of the same liquid was introduced. In comparison with other multiscale modelling literature, our method uses the modelling framework of a physical analogy to specify the coupling terms in the 'buffer' zone between the atomistic and hydrodynamic regions. Physical analogy methods for coupling models of different resolution have been used in continuum fluid dynamics for several decades. A classical example is the Lighthill acoustic analogy [36] which was introduced in continuum hydrodynamics to bridge the scale differences that span 3-4 orders of magnitude between the sound waves in the range of audible frequencies and the turbulent flow structures which generate sound. Since the original work of Lighthill [36], various hybrid methods of this kind were developed with a general idea to exactly rearrange the governing Navier-Stokes equations to the form of non-homogeneous linear equations for acoustic propagation ('coarse-grained' model)

and a non-linear source ('fine-scale' model). For most advanced approaches of this type (for example, [37, 38, 39]), the non-linear source is directly related to the properties of fine scale solution (the space and time scales of the turbulence). Following a similar line of thought, for multiscale modelling of the liquids across atomistic and hydrodynamic scales, in Markesteijn et al [12] the classical Buckley-Laverett filtration model [40] was considered in the context of a two-phase-flow analogy and implemented for 2D liquid argon simulations at high pressure conditions. In Scukins et al [41] the same two-phase flow analogy was extended to 2D water modelling where the Mercedes-Benz model [42] was used for the MD part of the solution. The idea of the hybrid method is to consider two representations of the same liquid, one is particles (atomistic) and one is Eulerian control cells (continuum) simultaneously. The particle and continuum parts of the solution were treated as 'phases' of the same liquid in accordance with the conservation laws. The communication was controlled by a user defined function of space and time $s(x, y)$ which described the influence of the representations on each other and had the meaning of partial concentration of the 'phases' in the two-phase-flow analogy. In comparison with the deterministic Navier-Stokes equations of the original Buckley-Laverett model, here the Landau Lifshitz Fluctuating Hydrodynamics (LL-FH) equations [43, 44] represent the continuum part of the solution in the current multiscale model based on the two-phase flow analogy.

The LL-FH equations allow for a correct statistical description of the collective properties of liquids including thermal fluctuations. Being Stochastic Partial Differential Equations (SPDE), the LL-FH equations are more numerically challenging in comparison with the deterministic Navier-Stokes equations. Notably, however, the LL-FH equations are still amenable to solution with Finite Differences [45, 46, 47], Finite Volumes [35, 48, 49], or the Lattice Boltzmann method [50, 51].

This publication is the first step in extending the hybrid multiscale model based on the two-phase flow analogy to 3D applications in the framework of a popular open source molecular dynamics software such as GROMACS [26]. Presently, a one-way coupling implementation is considered which is relevant to flow regimes when the continuum part of the solution does not require a feedback from the atomistic part and, thus, can be obtained from a separate hydrodynamics modelling.

The paper is organised as the following. In section 2, main equations of the hybrid multiscale approach based on the analogy with two-phase modelling are outlined (subsection 2.1), the current one-way coupling implementation is introduced (subsection 2.2), and numerical results are provided in section 3.

2. Hybrid multiscale hydrodynamics/molecular dynamics model

2.1 Governing equations of the two-way coupling model

Following Markesteijn et al [12], a nominally 'two-phase' (Molecular Dynamics (MD) and Landau-Lifshitz Fluctuating Hydrodynamics (LL-FH)) liquid model is considered as a representation of the same chemical substance. The 'phases' are immersed into each other as 'fine grains', the surface tension effects are irrelevant, and both parts of the solution simultaneously occupy the same cell in accordance with their partial concentrations. The partial concentration of the MD 'phase' and the LL-FH 'phase' is equal to s and $1-s$, respectively, where s is a parameter of the model $0 \leq s \leq 1$. In general s is a user-defined function of space and time which controls how much atomistic information is required in a particular region of the simulation domain.

Let's consider a solution domain of volume V_0 which is broken down into elementary Eulerian cubical cells of volume V. Each cell has 6 faces $\gamma = 1,..,6$ and it is filled with the continuum part of the liquid and, at the same time, with the MD particles which correspond to a discrete representation of the same chemical substance. It is assumed that the continuum part of the nominally two-phase fluid has the same transport velocity as that of the mixture. At isothermal condition this nominally two-phase liquid in addition to the macroscopic equation of state satisfies the following macroscopic conservation laws. For mass:

$$\delta_t(sm) + \sum_{\gamma=1,6}(s\rho\bar{\mathbf{u}})d\mathbf{n}^\gamma \delta t = \delta_t J^{(\rho)},\qquad\qquad\text{for the LL-FH phase, (1)}$$

$$\delta_t\left((1-s)\sum_{p=1,N(t)}m_p\right) + \sum_{\gamma=1,6}\left((1-s)\sum_{p=1,N_\gamma(t)}\rho_p\mathbf{u}_p\right)d\mathbf{n}^\gamma \delta t = -\delta_t J^{(\rho)},\;\text{ for the MD phase,}\qquad\text{(2)}$$

where m and $\rho = m/V$ are the mass and the density of the continuum 'phase' of the elementary volume V, m_p is the particle mass, $\mathbf{u}_p$ is the MD velocity, $\bar{\mathbf{u}}$ is the average velocity of the 'mixture' $\bar{u}_i = \left[s\rho u_i + (1-s)\sum_{p=1,N(t)}\rho_p u_{ip}\right]/\bar{\rho}$, u_i is the velocity of the continuum LL-FH 'phase', $\bar{\rho} = s\rho + (1-s)\sum_{p=1,N(t)}\rho_p$, $N(t)$ is the number of particles in the volume V. $N_\gamma(t)$ is the number of particles crossing the γth cell face with the normal $d\mathbf{n}^\gamma$, $\rho_p = m_p/V$ is the effective density of an MD particle p which occupies the volume V, and $\delta_t J^{(\rho)}$ is the mass source/sink term which describes the transformation of mass between the 'phases', δ_t describes the change of a quantity over time δt, e.g. the counters of particle mass and momentum in cell V accumulated over time δt.

For momentum this is:

$$\delta_t(smu_i) + \sum_{\gamma=1,6}\left(s\rho u_i\bar{\mathbf{u}}\right)d\mathbf{n}^\gamma\delta t = s\sum_{j=1,3}\sum_{\gamma=1,6}\left(\Pi_{ij}+\tilde{\Pi}_{ij}\right)dn_j^\gamma\delta t + \delta_t J_i^{(\mathbf{u})}, \tag{3}$$

$$\delta_t\left((1-s)\sum_{p=1,N(t)}m_p u_{ip}\right) + \sum_{\lambda=1,6}\left((1-s)\sum_{p=1,N_\gamma(t)}\rho_p u_{ip}\mathbf{u}_p\right)d\mathbf{n}^\gamma\delta t = (1-s)\sum_{p=1,N(t)}F_{ip}\delta t - \delta_t J_i^{(\mathbf{u})}, \tag{4}$$

where $\mathbf{\Pi}$ and $\tilde{\mathbf{\Pi}}$ are the deterministic and stochastic parts of the Reynolds stress tensor in the LL-FH model, F_{ip} is the MD force exerted on particle p due to the pair potential interactions, and $\delta_t J_i^{(\mathbf{u})}$ is the LL-FH/MD exchange term corresponding to the ith momentum component.

The sums of fluxes $\sum_{\gamma=1,6}\left((1-s)\sum_{p=1,N_\gamma(t)}\rho_p\mathbf{u}_p\right)d\mathbf{n}^\gamma\delta t$ and $\sum_{\lambda=1,6}\left((1-s)\sum_{p=1,N_\gamma(t)}\rho_p u_{ip}\mathbf{u}_p\right)d\mathbf{n}^\gamma\delta t$ are the corresponding counters of particle mass and momentum crossing the cell's boundaries $\gamma = 1,..,6.$

In theory, the flux terms can be calculated from the particle distributions at each point of the cell boundary. In practice, for computing the cell-boundary values an interpolation method can be used based on the particle distributions specified at the centres of adjacent volumes V, e.g. in a finite-volume framework.

By summing up the mass equations, (1) and (2) and assuming the conservation fluxes vanish at the domain boundaries, it follows from the divergence theorem that the mass conservation law for the mixture is exactly satisfied, $\bar{m}(t+\delta t) = \bar{m}(t), \ \bar{m} = \bar{\rho}V$. In a similar way, by combining the momentum equations, (3) and (4), it can be seen that the Newton second law, which equates the change of the total momentum $\bar{m}\cdot\bar{\mathbf{u}}$ to the force applied, $\bar{F}_i = s\sum_{j=1,3}\sum_{\alpha=1,6}\left(\Pi_{ij}+\tilde{\Pi}_{ij}\right)dn_j^\alpha\delta t + (1-s)\sum_{p=1,N(t)}F_{ip}$, is satisfied. Note that the latter expression for

9

the force applied in the hybrid system is similar to the interpolation used in the original AdResS method [32] for particle-particle interaction.

In (1)-(4), $\partial_t J^{(\rho)}$ and $\partial_t J_i^{(\mathbf{u})}$ are the user defined functions which need to be specified to close the model. These functions can be obtained from specifying how fast the mixture averaged values $\bar{\rho}$ and $\bar{u}_i \bar{\rho}$ should equilibrate to the cell averaged parameters from the MD 'phase' of the simulation, $\sum_{p=1,N(t)} m_p$ and $\sum_{p=1,N(t)} u_{ip} m_p$:

$$D_t \left(\bar{m} - \sum_{p=1,N(t)} m_p \right) = L^{(\rho)} \bullet \left(\bar{m} - \sum_{p=1,N(t)} m_p \right),$$

$$D_t \left(\bar{u}_i \bar{m} - \sum_{p=1,N(t)} u_{ip} m_p \right) = L^{(u)} \bullet \left(\bar{u}_i \bar{m} - \sum_{p=1,N(t)} u_{ip} m_p \right) + s \sum_{j=1,3} \sum_{\gamma=1,6} \left(\Pi_{ij} + \tilde{\Pi}_{ij} \right) dn_j^\gamma \delta t,$$

(5)

where,

$$D_t \left(\bar{m} - \sum_{p=1,N(t)} m_p \right) = \delta_t \left(\bar{m} - \sum_{p=1,N(t)} m_p \right) + \sum_{\gamma=1,6} \left(\bar{\rho} - \sum_{p=1,N_\gamma(t)} \rho_p \right) \mathbf{u} d\mathbf{n}^\gamma \delta t,$$

$$D_t \left(\bar{u}_i \bar{m} - \sum_{p=1,N(t)} u_{ip} m_p \right) = \delta_t \left(\bar{u}_i \bar{m} - \sum_{p=1,N(t)} u_{ip} m_p \right) + \sum_{\gamma=1,6} \left(\bar{u}_i \bar{\rho} - \sum_{p=1,N_\gamma(t)} u_{ip} \rho_p \right) \mathbf{u} d\mathbf{n}^\gamma \delta t,$$

(6)

are integral analogues of the full conservative derivatives in the case of smooth variable fields using the divergence theorem, and, using the same theorem, the operators at the right-hand side of

$$L^{(\rho)} \bullet \left(\bar{m} - \sum_{p=1,N(t)} m_p \right) = \sum_{k=1,3} \sum_{\gamma=1,6} \left(s(1-s) \cdot \alpha \cdot \frac{1}{V} \left(\sum_{\lambda=1,6} \left(\bar{\rho} - \sum_{p=1,N_\lambda(t)} \rho_p \right) dn_k^\lambda \right) \right) dn_k^\gamma \delta t,$$

$$L^{(u)} \bullet \left(\bar{u}_i \bar{m} - \sum_{p=1,N(t)} u_{ip} m_p \right) = \sum_{k=1,3} \sum_{\gamma=1,6} \left(s(1-s) \cdot \beta \cdot \frac{1}{V} \left(\sum_{\lambda=1,6} \left(\bar{u}_i \bar{\rho} - \sum_{p=1,N_\lambda(t)} u_{ip} \rho_p \right) dn_k^\lambda \right) \right) dn_k^\gamma \delta t,$$

(7)

are integral analogues of the corresponding second order diffusion derivative.

In the above equations, $\alpha, \beta > 0$ are two adjustable parameters, which characterise how fast the two 'phases' equilibrate to the same macroscopic condition, i.e. converge to the same liquid they represent. The characteristic relaxation time associated with these parameters $\tau^{diff} \sim \Delta x^2 / \alpha \sim \Delta x^2 / \beta$, where $\Delta x \sim V^{-1/3}$ is the length scale associated with the cell volume V, should be comparable to the time step of the particles $\tau^{diff} \sim \tau^{MD}$ so that the relaxation process affects the particle trajectories over their characteristic time scale (also see the modified MD equations in the hybrid MD/LL-FH zone below). For example, for too small values of the relaxation parameters α, β, the MD part of the simulation runs away from the continuum part which leads to divergence of the atomistic part of the solution from the continuum one. For too large values of the coupling parameters, the system of equations becomes too stiff and numerically unstable.

To close the model, (5)-(7) are combined with the following equations of mass and acceleration for the particles in each Eulerian cell

$$\delta_t \sum_{p=1,N(t)} m_p + \sum_{\gamma=1,6} \left(\sum_{p=1,N_\gamma(t)} \frac{d\mathbf{x}_p}{dt} \rho_p \right) d\mathbf{n}^\gamma \cdot \delta t = 0,$$

$$\delta_t \sum_{p=1,N(t)} m_p u_{ip} + \sum_{\gamma=1,6} \left(\sum_{p=1,N_\gamma(t)} \frac{d\mathbf{x}_p}{dt} \rho_p u_{ip} \right) d\mathbf{n}^\gamma \cdot \delta t = \sum_{p=1,N(t)} m_p a_{ip} \delta t, \quad a_{ip} = \frac{du_{ip}}{dt},$$

$\qquad\qquad$ (8)

which defines the source/sink terms in (1)-(4) and the modification to MD particle equations for velocity and acceleration, $\frac{d\mathbf{x}_p}{dt} = \mathbf{u}_p, \frac{d\mathbf{u}_p}{dt} = \mathbf{F}_p$ as the following:

$$\frac{d\mathbf{x}_p}{dt} = \mathbf{u}_p + s(\bar{\mathbf{u}} - \mathbf{u}_p) + s(1-s)\cdot\alpha\cdot\frac{\sum\limits_{\gamma=1,6}\left(\bar{\rho} - \sum\limits_{q=1,N_\gamma(t)}\rho_q\right)d\mathbf{n}^\gamma}{\sum\limits_{q=1,N(t)}m_q},$$

$$\frac{du_{ip}}{dt} = (1-s)F_{ip}/m_{ip} +$$

$$+ \sum_{k=1,3}\sum_{\gamma=1,6}\left(s(1-s)\cdot\alpha\cdot\sum_{q=1,N_\gamma(t)}\rho_q u_{iq}\cdot\left(\frac{\sum\limits_{\lambda=1,6}\left(\bar{\rho} - \sum\limits_{q=1,N_\lambda(t)}\rho_q\right)dn_k^\lambda}{\sum\limits_{q=1,N(t)}m_q}\right)\right)dn_k^\gamma/\sum_{q=1,N(t)}m_q \qquad (9)$$

$$+ \sum_{k=1,3}\sum_{\gamma=1,6}\left(s(1-s)\cdot\beta\cdot\frac{1}{V}\left(\sum_{\lambda=1,6}\left(\bar{\rho}\cdot\bar{u}_i - \sum_{q=1,N_\lambda(t)}\rho_q u_{iq}\right)dn_k^\lambda\right)\right)dn_k^\gamma/\sum_{q=1,N(t)}m_q, \qquad i = 1,3,$$

where the macroscopic fields $\bar{\rho}$, $\bar{\mathbf{u}}$, $\sum\limits_{q=1,N(t)}\rho_q$ and $\sum\limits_{p=1,N(t)}\rho_q\mathbf{u}_q$ correspond to cell-average values at

each location $\mathbf{x}$ of MD particle p. For a practical computation, the values of these fields can be

determined by interpolation, in the same way as the cell-face fluxes in equations (1)-(4).

Derivation details are given in Appendix A.

Notably, the modified MD equations (9) depend only on the mixture conservation variables

and the cell-averaged MD solution. For the numerical implementation, it is convenient to solve

(9) together with the conservation equations for the mixture density and momentum, (5)-(7),

rather than the original equations (1)-(4) which become degenerate in the limit of $s = 0$ or $s = 1$.

Because of the stochastic stresses included, equations (5)-(7) are Stochastic Partial Differential

Equations, similar to Landau-Lifshitz Fluctuating Hydrodynamics (LL-FH) equations which are

their limiting case. Indeed, in the case when the continuum 'phase' is the only part of the hybrid

model (i.e. when $s = 1$ and when there are no MD particles), the equations (5)-(7) for the mixture

density and momentum reduce to the classical Landau-Lifshitz Fluctuating Hydrodynamics equations.

In addition to the conservation of mass and momentum of the 'mixture', the model (5)-(7) also directly satisfies the Fluctuation Dissipation Theorem (FDT) in the limiting states when $s = 0$ and $s = 1$, that is for the pure MD and the pure LL-FH equations. In the hybrid MD/LL-FH region, assuming the two parts of the solution are fully relaxed to the same macroscopic state, the diffusion terms that are proportional to the discrepancy between the MD part of the solution from the 'LL-FH' part vanish and the coupling terms of the hybrid model (9) just become a linear combination of the LL-FH and the cell-averaged MD velocities and forces, hence, satisfy the FDT because of the linearity. In practice, the assumption of full relaxation of the two 'phases' to the same macroscopic state needs an a posteriori confirmation. Such confirmation will also be reported in the results section of the paper.

2.2. Simplified one-way coupling model

For the sake of the implementation in this paper, we will only consider macroscopically stationary liquids in the absence of any hydrodynamic gradients and away from solid boundaries. Under such assumptions, thermal fluctuations are the only source of macroscopic fluctuations in liquids described by the LL-FH model.

Therefore, we assume that equations of the 'two-phase mixture' (5) and (6) are completely decoupled from the MD 'phase' and the corresponding conservation variables, $\bar{\rho}$ and $\bar{u}_i$, which drive the MD equations (9), can be obtained from a separate hydrodynamics calculation. As discussed in section 2.1, it is the LL-FH equations which need to be solved in this case:

13

$$\frac{\partial \bar{\rho}}{\partial t} + div(\bar{\rho} \cdot \bar{\mathbf{u}}) = 0,$$

$$\frac{\partial(\bar{\rho} \cdot \bar{u}_i)}{\partial t} + div(\bar{\rho} \cdot \bar{u}_i \cdot \bar{\mathbf{u}}) = \sum_{j=1,3} \nabla_j \left(\Pi_{ij} + \tilde{\Pi}_{ij} \right), \quad i = 1, 2, 3 \tag{10}$$

where the Equation Of State (EOS), $\bar{p} = \bar{p}(\bar{\rho})$ and the shear and bulk viscosity coefficients, η

and ζ, which enter the Reynolds stress $\mathbf{\Pi}$ and its fluctuating component $\tilde{\mathbf{\Pi}}$,

$$\Pi_{i,j} = -\left(\bar{p} - \zeta div\bar{\mathbf{u}}\right)\delta_{i,j} + \eta\left(\partial_i\bar{u}_j + \partial_i\bar{u}_j - 2D^{-1}div\bar{\mathbf{u}}\delta_{i,j}\right),$$

$$\tilde{\Pi}_{i,j} = \zeta div\tilde{\mathbf{u}}\delta_{i,j} + \eta\left(\partial_i\tilde{u}_j + \partial_i\tilde{u}_j - 2D^{-1}div\tilde{\mathbf{u}}\delta_{i,j}\right), \quad i,j = 1, 2, 3 \tag{11}$$

need to be defined in accordance with the MD model as will be discussed in section 2.3.

In the above equations, the stochastic stress tensor $\tilde{\mathbf{\Pi}}$ is described as a random Gaussian

matrix with zero mean and covariance, given by the formula:

$$\left\langle \tilde{\Pi}_{i,j}(\mathbf{r}_1, t_1)\tilde{\Pi}_{k,l}(\mathbf{r}_2, t_2) \right\rangle = 2k_B T \left[\eta\left(\delta_{i,k}\delta_{j,l} + \delta_{i,l}\delta_{j,k}\right) + \left(\zeta - 2D^{-1}\eta\right)\delta_{i,j}\delta_{k,l} \right] \delta(t_1 - t_2)\delta(\mathbf{r}_1 - \mathbf{r}_2). \tag{12}$$

Using this correlation, the stochastic stress tensor can be expressed explicitly as [43]:

$$\tilde{\Pi}_{i,j} \cong \sqrt{\frac{2k_B T}{\delta t \delta V}} \left(\sqrt{2}\sqrt{\eta} \cdot G_{i,j}^S + \sqrt{D}\sqrt{\zeta} \cdot tr[\mathbf{G}] \cdot E_{i,j} / D \right), \quad i,j = 1, 2, 3 \tag{13}$$

where $\mathbf{G}$ is a random Gaussian matrix with zero mean and covariance $\left\langle G_{i,j}G_{k,l} \right\rangle = \delta_{i,j}\delta_{k,l}$,

$G_{i,j}^S = \dfrac{G_{i,j} + G_{i,j}^T}{2} - tr[\mathbf{G}] \cdot E_{i,j} / D$, is a random symmetric matrix with zero trace, $\mathbf{E}$ is the

identity matrix, and $tr[\mathbf{G}]$ is the trace of the matrix $\mathbf{G}$.

For the current one-way coupling implementation of the hybrid multiscale model, the LL-FH

equations (10)-(13) are solved together with the MD equations (9). The MD particles are present

everywhere in the solution domain including the hydrodynamics dominated zone where the

periodic boundary conditions are specified. For a large size of the LL-FH zone, the current

implementation can still be made efficient in comparison with the all-atom simulation since the cost of the LL-FH model in comparison with the MD simulation is negligible. For example, in MD computing the interaction potentials scale as $N \log N$, where N is the number of MD particles. The reduction of the computational cost for the hybrid model in comparison with the all-atom simulation can be up to $\log N$. Further computational savings can be achieved by introducing spatially variable space-time scales into the simulation with expansion from fine atomistic to large hydrodynamic scales where the MD particles would lose their mobility because of small thermal fluctuations in large cell volumes, and, thus, could be constrained to a small part of the solution domain. This work is underway.

To complete the model description, the 'partial concentration' function $s=s(x,y,z)$ needs to be specified. Here, two types of the s function are considered: (i) a constant field across the whole system as in [12, 18] for 2D modelling and (ii) a zoom-shape function allowing to vary the model resolution based on a user defined geometrical shape of $s(x,y,z)$, which can be viewed as a 3D version of the circular zone considered in [41]. For the latter, two types of the variable s-function were used. In one, s varies along the x direction only, $s = s(x)$, and in the other it has a spherical symmetry (fig.1):

$$s(x,y,z) = \begin{cases} S_{min}, & r \leq R_{MD}; \\ \dfrac{r - R_{MD}}{R_{FH} - R_{MD}}(S_{max} - S_{min}) + S_{min}, & R_{MD} < r < R_{FH}; \\ S_{max}, & r \geq R_{FH}. \end{cases} \qquad (14)$$

where $r = (x-L/2)^2 + (y-L/2)^2 + (z-L/2)^2$, L is the computation box size, $x,y,z \in [0,L]$, $S_{min} = 0$, $S_{max} = 1$.

In Fig. 1, the red region with water molecules is the purely atomistic domain that gradually changes through white (hybrid atomistic-continuum region) to blue (purely fluctuating hydrodynamics region).
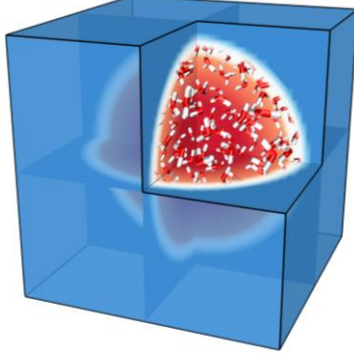

Figure 1. Variable *s* parameter and MD sphere inside the computation box. The red zone is the pure MD region ($s = 0$), while the blue is the fluctuating hydrodynamics region ($s = 1$) for the spherically symmetrical s-function case.

2.3 Numerical details of solving the continuum fluid dynamics equations and communication with the MD part of the solution

The LL-FH equations are solved in the conservation form (11) and (13) with the two-time-level modification of the Central Leapfrog scheme from [47]. The modified Central Leapfrog scheme uses a low dissipative nonlinear flux correction for stability. It is simple for implementation and, despite this, accurately predicts the correct value for the thermal fluctuations on par with the most accurate three stage Runge–Kutta methods such as in [46, 52]. However, in comparison with the latter scheme the computational cost of the current single stage Central Leapfrog scheme is about 3 times smaller.

For solving the LL-FH equations, the case specific Equation of State (EOS) is important for coupling the continuum equations with the MD solution [47]. However, unlike the continuum LL-FH domain, the EOS of the MD domain is a result of the simulation rather than a relation prescribed as the model input. Therefore, to ensure similar behaviour in both domains, a separate MD simulation is used to determine the EOS of the investigated fluid. In the current work, the method of determining EOS from [47] is used, which consists of the following steps: 1) several all-atom MD simulations are performed with different average density; 2) in these simulations the pressure of the system is calculated using the Irving and Kirkwood expression for pressure [53]; 3) a polynomial fit is done on the resulting pressure versus density curve; 4) the polynomial fit is substituted in the Reynolds stress tensor of the LL-FH equations.

In addition to the EOS, there are other important parameters that need to be specified for the LL-FH domain, namely, the values for the shear and bulk viscosities. Similarly to the EOS, the viscosity of the MD fluid is a result of the simulation rather than an input parameter. Therefore, the value obtained from an MD simulation is used as an input parameter for the LL-FH domain. The computation of viscosity coefficients of water needs a special attention. Indeed, as it is known from literature, the viscosity is computed when using water models is not the same as the experimental value of water [54, 55, 56, 57, 58]. Therefore, it is the viscosities which correspond to the particular MD water models rather than the experimental values are used in the continuum model as mentioned in Table 1. The values for the shear and bulk viscosities for argon are less sensitive to the MD modelling and in this work they are taken from [48].

The computation of new coordinates and velocities of atoms in (7) consists of two stages: (i) obtaining the cell-averaged field variables $\bar{\rho}$ and $\bar{u}_i$ from the solution of the LL-FH equations as well as the corresponding cell-averaged quantities $\sum_{p=1,N(t)} \rho_p$ and $\sum_{p=1,N(t)} u_{ip}\rho_p$ from the MD

particles which are also averaged in time to be compatible with the hydrodynamics variables and (ii) reconstruction of the continuously varying distributions of the field variables inside each LL-FH cell to be used in the MD particle equations (9).

For consistency with the numerical solution of continuum equations (11) and (13), which correspond to a certain time step, or time-averaging in accordance with the hydrodynamics time scale, that is 10 times larger than the MD time step for the present hybrid model, the cell-averaged MD fields $\sum_{p=1,N(t)} \rho_p$ and $\sum_{p=1,N(t)} u_{ip} \rho_p$ should also be averaged in time accordingly. Although this is standard practice when continuum information is extracted from MD simulations, inconsistencies occur when the sampling is taken over too few atoms or too small cell sizes [49]. The main reason for this is the fact that the sampling only takes into account the coordinate of the centre of mass of every atom, which is directly translated to a (single) discrete LL-FH cell index. This makes perfect sense from a molecular point of view, as the nucleus (and not the electron cloud) accounts for almost all the atom's mass and therefore most of the mass would be in a single LL-FH cell. However, when the fluctuations are examined on a per cell basis using this simple sampling technique, the statistics of these fluctuations do not match the continuum observables [49, 59]. A straightforward method that can be applied to match the continuum observables extracted from all atom simulations is to use so-called mapping techniques [49, 59]. By using such a technique, each atom or molecule is taken into account as a cubical blob having a centre that corresponds to the centre of mass of the atom or molecule, and a corresponding side length d that can be tuned such that the continuum observables match. However, as is further explained in [59], different blob sizes should be used for different continuum observables (mass and momentum). Additionally, the consistent scaling and the most appropriate blob size also depend on the type of atom or molecule, e.g. argon or water [59].

The numerical simulations in this paper deal with argon and SPC/E water and the blob filtering technique as discussed in [49] is used to map the atom coordinates to continuum field approximations. For every molecule the centre of mass and the velocity of the centre of mass are computed. During mapping the fraction C of each cubical blob with size d in the LL-FH cells is calculated, where the centre of the blob coincides with the centre of mass of the molecule. This means that the contribution of each blob to cell density and cell momentum is directly proportional to the fraction C of the blob. The filter works three dimensionally and assumes periodic boundary conditions everywhere. The size of the cubical blob for argon is taken as 0.28 nm, while the size of the cubical blob for SPC/E water is taken as 0.18 nm. These values gave the best results in our case and are within the range of values given in [59]. However, the values are slightly different than the optimal values reported in [59]. The reason for the difference could be the fact that the equations solved here are under isothermal conditions, i.e. no energy equation is solved explicitly.

Once the continuum density and velocity variables, including the MD fields, are obtained as the cell-averaged parameters, the corresponding continuous fields need to be reconstructed inside each cell for solving (9). The continuity of the reconstructed fields is important for the hydrodynamic forces acting on the MD particles to remain bounded across the boundaries of the LL-FH cells. For the current implementation, a tri-cubic interpolation method is used which ensures that the reconstructed solutions are not only continuous but also smooth, so that the forces which are proportional to the solution gradient are not only bounded but also continuous across the cell boundaries.

Both the LL-FH equations (11) and (13) and the modified MD equations (9) have been implemented as internal procedures of the GROMACS 5.0 package for three cases: argon,

SPC/E water, and a peptide system. The general parameters used in the MD and LL-FH parts of the simulations are given in Table 1. For all simulations a constant temperature (NVT) ensemble was used with the Nosé-Hoover thermostat [60, 61] available in GROMACS. The boundary conditions in all cases were periodic. For the water models, LINCS algorithm [62] was used to constrain the bonds.

Table 1. Simulation parameters used in GROMACS for argon and SPC/E water and the viscosity values used in the LL-FH code

	Argon	Argon (acoustic wave test)	SPC/E Water
Number of atoms (molecules)	64000	32000	91125 (30375)
Molecular mass (g mol^{-1})	39.948	39.948	18.015
Temperature, (K)	300	300	298.15
Box volume, (nm^3)	16.21x16.21x16.21	32.424x8.106x8.106	9.686x9.686x9.686
MD time step, (ps)	0.01	0.01	0.001
α, β, (nm^2 ps^{-1})	1000	1000	5000
Blob size, (nm)	0.28	0	0.18
Average density (amu nm^{-3})	600.24	600.0	602.18
Shear viscosity (amu nm^{-1} ps^{-1})	54.74	54.74	409.496
Bulk viscosity (amu nm^{-1} ps^{-1})	18.23	18.23	933.41

In what follows, the performance of the hybrid model for a range of constant parameter s = const values throughout the solution domain is discussed first. Then, the results of the truly multiscale version of the same model are discussed when the coarse graining parameter s becomes a function of geometrical location in accordance with (14). The focus of attention here are both in the microscopic solution details such as in Radial Distribution and Velocity Autocorrelation Functions and the macroscopic characteristics such as mean values and standard

deviation of density and velocity. The capability of the current hybrid model in the hybrid MD/LL-FH zone to satisfy the correct mass and momentum balance and fluctuations will be probed as well as to correctly preserve the autocorrelation of density and velocity in accordance with the Fluctuation Dissipation Theorem and to the transport hydrodynamics fluctuations such as for acoustic wave travelling from the LL-FH to MD part of the domain through the intermediate hybrid zone. Finally, an example of using the current hybrid MD/LL-FH method for computing the diffusion of water and a small peptide dialanine in water will be provided.

3. Results

3.1. Hybrid simulations of argon and water: constant *s*-function

The results of the simulation of liquid argon at high pressure conditions are presented first. One very important property to match [47, 52] is the standard deviation of density and velocity for the LL-FH and the MD part of the solution. In accordance with the theory, the standard deviations of the velocity and density fluctuations corresponding to the equations (15) and (16) are:

$$STD(\rho') = c_T^{-1}\sqrt{\rho k_B \frac{T}{V_{cell}}}, \tag{15}$$

$$STD(u') = \sqrt{k_B \frac{T}{\rho V_{cell}}}, \tag{16}$$

where V_{cell} is the cell volume, T and ρ are the temperature and density, while c_T is the isothermal speed of sound.

Figure 2 shows the standard deviation (STD) of the velocity fluctuations for argon for several cases. The considered cases are: pure MD ($s = 0$) using just a simple sampling technique without the blob filter, the MD part of the solution for two intermediate cases with constant $s = 0.1$ and

s = 0.8, and the LL-FH solution. As can be concluded from the figure the velocity fluctuations in all cases converge to the same value (~0.011 nm/ps) within approximately 3 ns. From this it is also evident that the blob filter is not necessary in order to obtain better matching of the velocity fluctuations. The theoretical value of the velocity STD for argon according to (15) is 0.0110 nm/ps.

Figure 3 shows the standard deviation of the density fluctuations for argon for the same cases and for the pure MD case with the blob filter enabled. Again, all cases, except for the pure MD without the blob filter, the value converge to the same value (~10.7 amu/nm^3) which is in good agreement with the theoretical value of 10.52 amu/nm^3 for argon according to Eq. (15). As expected the value for the density fluctuations without the blob filter are significantly overestimated that clearly shows the need for the filter in order to get the correct values of density fluctuations.
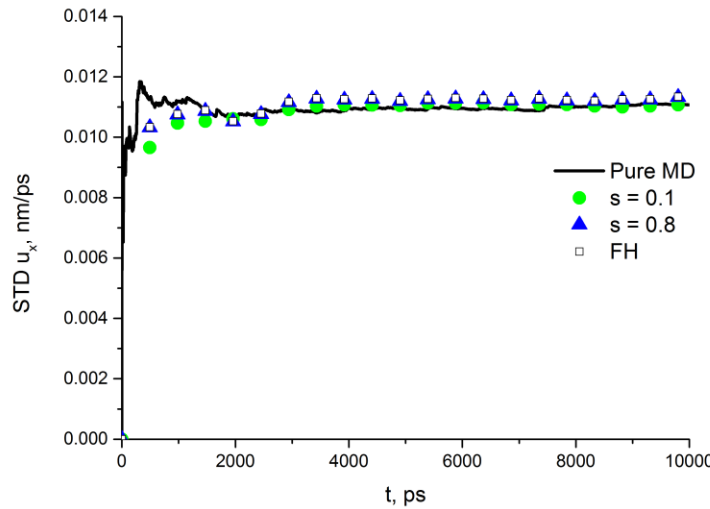
Figure 2. Standard deviation of the velocity fluctuations for argon for four different cases; pure MD solution (*s* = 0) without a blob filter, MD part of the solution for *s* = 0.1 and *s* = 0.8, and LL-FH solution
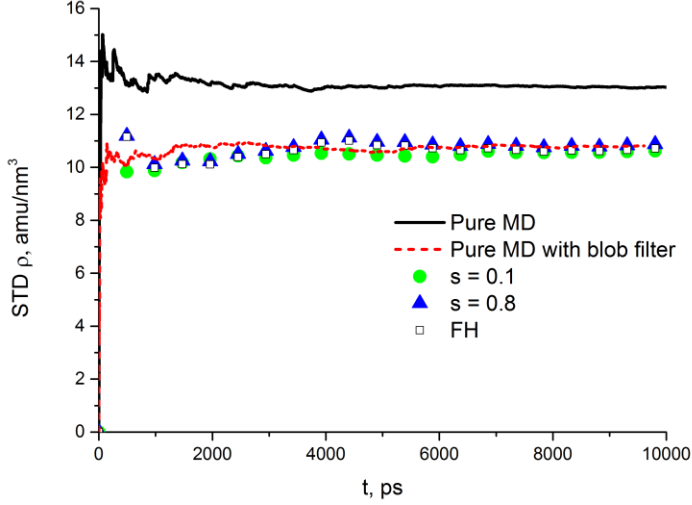
Figure 3. Standard deviations of the density fluctuations for argon for five different cases; pure

MD solution ($s = 0$) without and with a blob filter, MD part of the solution for $s = 0.1$ and

$s = 0.8$, and LL-FH solution

The actual value of the isothermal speed of sound c_T can be obtained from the relationship

between Eq. (10) and (11):

$$c_T = \rho \frac{STD(u')}{STD(\rho')}.$$ (17)

According to Eq. (17) and the results from the simulations, the simulated speed of sound for

argon is approximately 0.617 nm/ps. The theoretical value can be determined from the equation

of state [47] which evaluates to 0.63 which is in 2 percent agreement with the numerical

estimation.

Besides the fluctuations, two other important properties to examine are the radial distribution

function (RDF) and the velocity autocorrelation functions (VACF). Figure 4 shows the RDF as

obtained for different MD/LL-FH cases, here s is changed from constant $s = 0$ (pure MD), constant $s = 0.1$, 0.5, and 0.9 and, for comparison, also varies in accordance with (14) where only the atoms inside the MD sphere were used. As is evident from the figure, the accuracy of RDF is not affected by introducing the hydrodynamic component into the solution. Since RDF can be associated with density at micro scale, this means that the current hybrid coupling procedure does not affect the distribution of atoms preserving the effective density of the liquid regardless of the continuum 'phase' concentration.
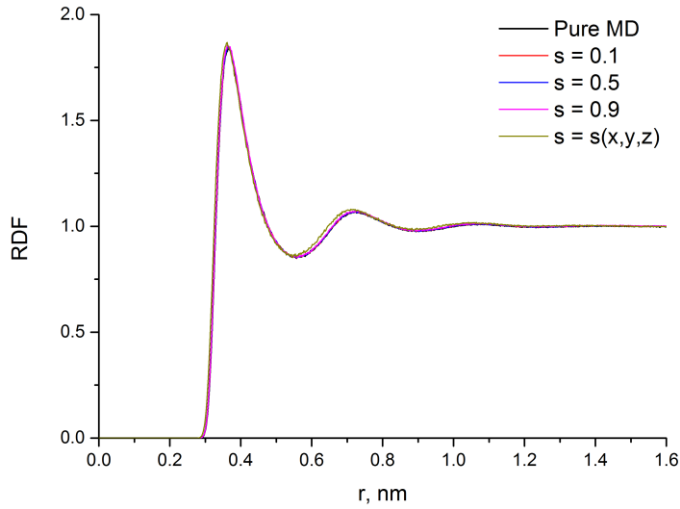
Figure 4. Radial distribution functions for different s values for argon

Figure 5 represents the velocity autocorrelation functions (VACF) for different constant s values for argon in comparison with each other, the pure MD ($s = 0$), and the pure LL-FH ($s = 1$) cases. It is shown that for the hydrodynamics dominated (large s) cases the velocities are highly correlated unlike for the atomistic dominated (small s) case. The curves for intermediate s

24

smoothly tend from the pure MD solution to the pure LL-FH solution while *s* is increasing from 0.1 to 1.
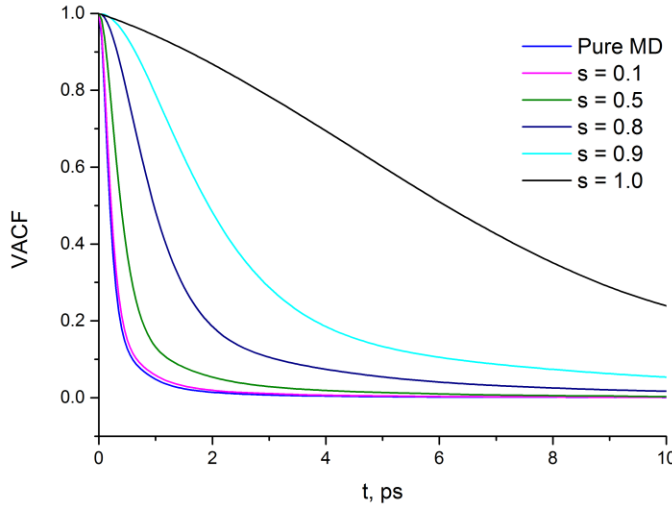
Figure 5. Velocity autocorrelation functions for different constant *s* values for argon

The results for SPC/E water modelling are presented next. First, the fluctuations are compared: Figures 6 and 7 show the standard deviations of the velocity and density fluctuations for SPC/E water. Again, the velocity STDs for pure MD, LL-FH, and the MD part of the hybrid solution converge to a value of approximately 0.023-0.024 nm/ps. This is in very good agreement with the theoretical prediction of 0.0238 nm/ps according to the theory (16). On the other hand, similar to the case of argon, the density STD for pure MD water simulations is noticeably overestimated. By introducing the blob filter with the blob size of 0.18 nm a much better STD prediction is obtained, approximately 9.8-10.2 amu/nm^3 compared to the theoretical value of 10.06 amu/nm^3).
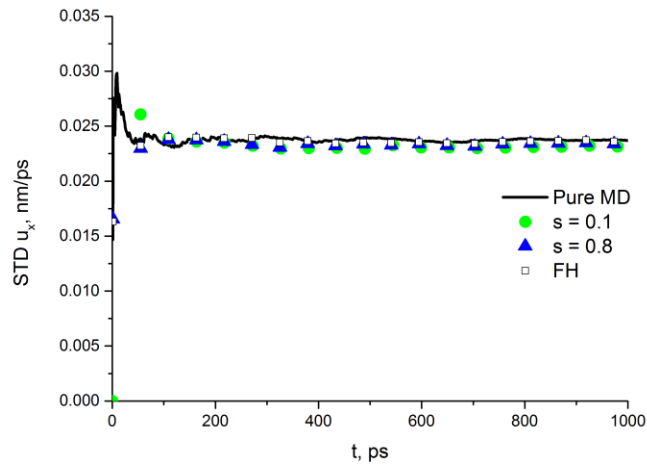
Figure 6. Standard deviations of the velocity fluctuations for SPC/E water for four different

cases; one pure MD case ($s = 0$), two MD/LL-FH cases with $s = 0.1$ and $s = 0.8$, and pure LL-FH

case ($s = 1$)
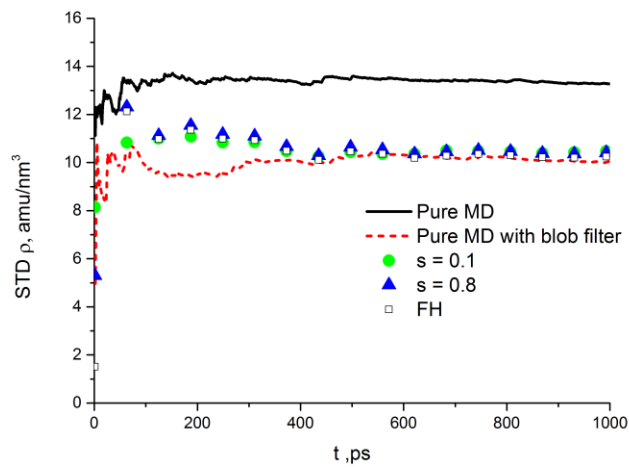
Figure 7. Standard deviations of the density fluctuations for SPC/E water for five different

cases: pure MD solution ($s = 0$) without a blob filter, MD part of the solution for $s = 0.1$ and

$s = 0.8$, and LL-FH solution

26

3.2. Hybrid simulations of argon and water: variable s-function

To investigate the effect of the hybrid MD/LL-FH zone on the accuracy of the atomistic part of the model for the case of variable s in the spherical domain described by Eq(14) the Velocity Auto Correlation Function (VACF) of argon is calculated next. Only those particles which are inside the MD sphere where $s = 0$ are accounted for in the VACF calculation. Figure 8 shows that the resulting VACF curve has a similar shape as the pure MD VACF. The velocities inside the MD region look slightly more correlated than those of the reference pure MD (all-atom) solution. This is most likely the effect of the relatively small MD sphere and high influence of the LL-FH region that can induce collective movements on the MD particles in the MD region.

To reduce those movements, further work will be devoted to implementing a larger LL-FH simulation box which corresponds to a larger buffer zone between the pure MD sphere and the LL-FH regions as well as introducing a more gradual transition from the fine space-time atomistic scales in the domain centre to the large space-time hydrodynamic scales at the boundaries of the LL-FH domain, for example, using the spatially variable time integration approach as discussed in [63].
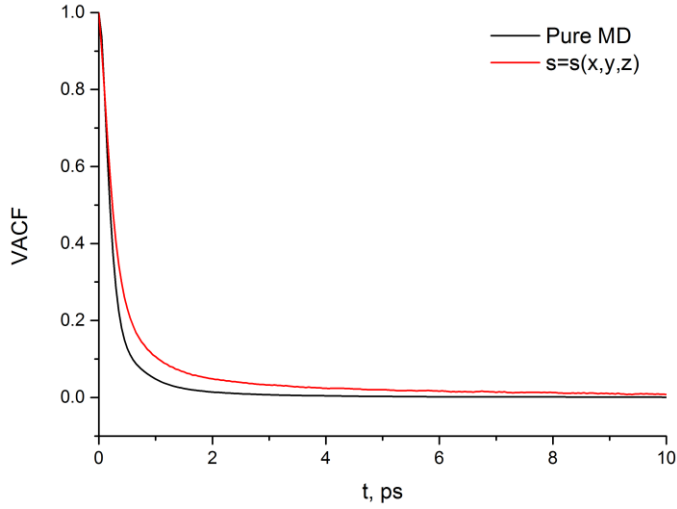
Figure 8. Velocity autocorrelation functions in the case of variable *s* for argon

Next, the RDF and VACF are computed for SPC/E water, for the variable *s* case in accordance with (14). Figure 9 shows a snapshot of the SPC/E water simulation for this case. A cross section of the simulation box where the central sphere represents the MD region with white and red water molecules surrounded by blue spheres that represent the heavier and slower hydrodynamics dominated particles (water blobs) is shown. Note that the hydrodynamics dominated water blobs in the figure are represented by spheres purely for clarity in showing the transition zone between MD and LL-FH. In reality these blobs are also water molecules, where the relative weight of the MD or LL-FH equations is given by the *s*-value in accordance with the hybrid MD/LL-FH model.
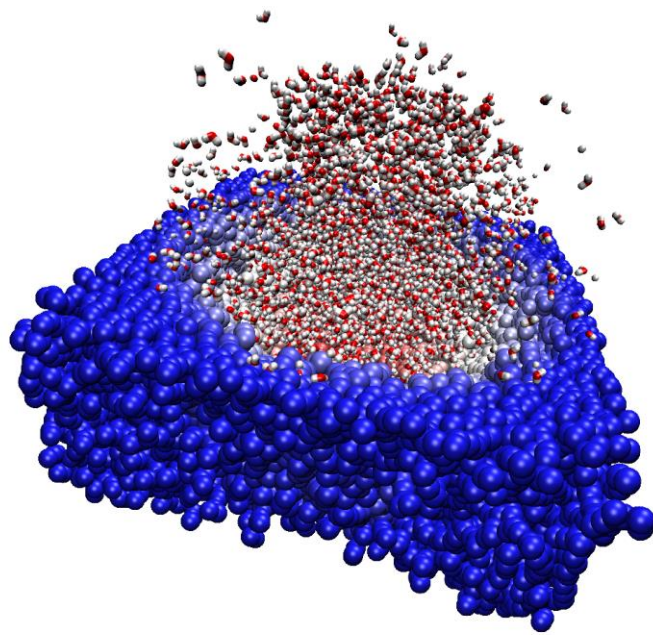
Figure 9. A cross section of the simulation box with SPC/E water in the case of the variable s simulation; the white and red molecules are water molecules in the MD region, the blue spheres are the water blobs in the region dominated by hydrodynamics

Figures 10 and 11 show the radial distribution functions for water (O-H and O-O pairs) for different s parameters including the case with variable s as compared with the all-atom simulation (pure MD). For the variable s case, the corresponding solution inside the MD sphere ($s = 0$) is shown. Similarly to the results obtained for argon, it can be concluded that the space distribution of water atoms is well preserved for both constant s and in the MD region when s is variable.
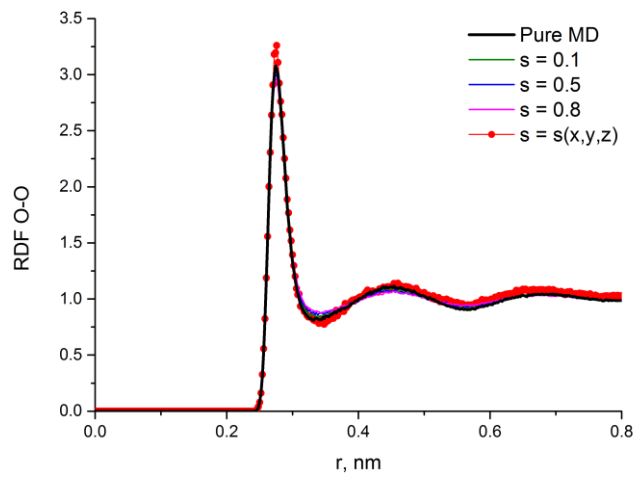
Figure 10. Radial distribution functions Oxygen-Oxygen for different *s* values for SPC/E water
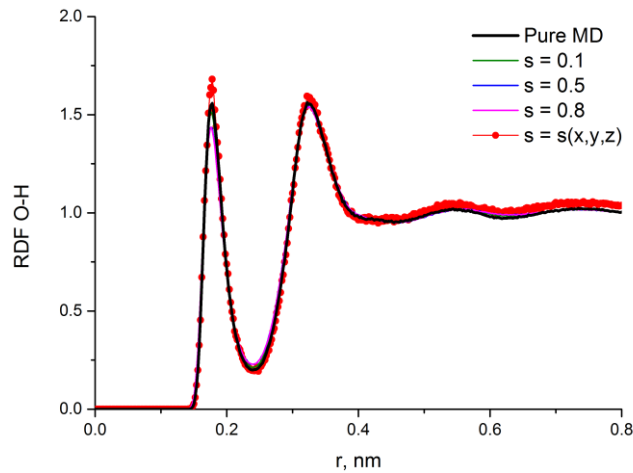
Figure 11. Radial distribution functions Oxygen-Hydrogen for different *s* values for SPC/E
water

Figure 12 represents the velocity autocorrelation functions for water for different constant *s* parameters. Here, unlike the argon case, the water VACFs have local minima and maxima. For

values of *s* approaching 1, the VACFs become stretched along the time axis and tend to the LL-FH curve.
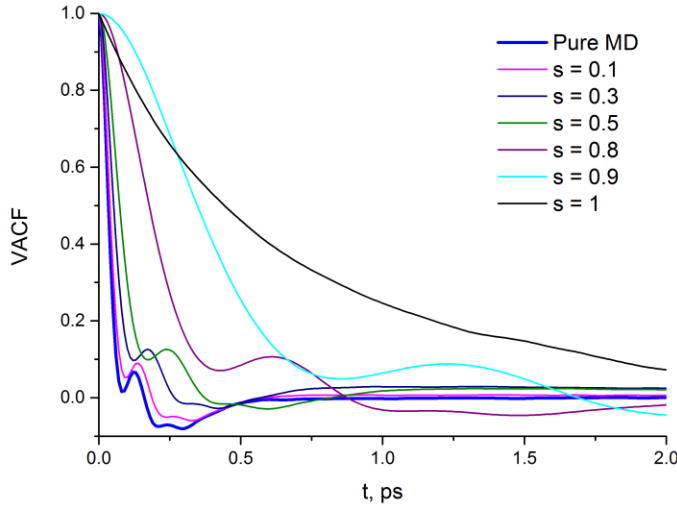
Figure 12. Velocity autocorrelation functions for different constant *s* values for SPC/E water

The VACF of water inside the MD region in the case of variable *s* in comparison with the pure MD case is shown in Figure 13. It can be noticed that for the first 0.06-0.07 ps the functions are the same. After 0.07 ps the curves are slightly different due to the finite MD sphere size but the shape is very similar. This means that for variable *s* in the MD sphere with $s = 0$, the microscopic statistical properties of water are preserved: both in terms of RDFs and VACFs.
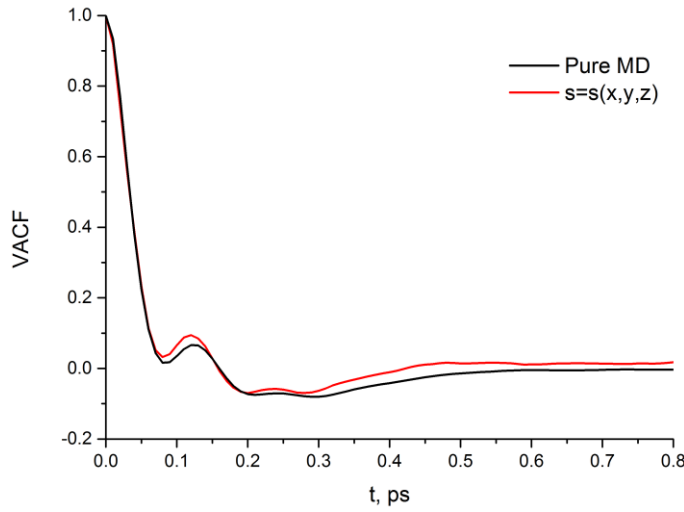
Figure 13. Velocity autocorrelation functions in the case of variable *s* for SPC/E water

Next, the continuity of the density and momentum fields as well as their fluctuations in the hybrid MD/LL-FH zone $0 < s < 1$ are investigated and compared with the theoretical solution. For the mixture variables of the current one-way coupling model, $\bar{\rho}$ and $\bar{u}_i$, which correspond to the solution of the LL-FH equations (11) and (13), the continuity and correct fluctuations are guaranteed as discussed in section 2.3. Hence, it is the MD part of the solution that remains in the focus of current investigation.

Figures 14 and 15 show the variation of density, momentum and their standard deviations for the MD part of the solution, $\rho_{MD} = \sum\limits_{p=1,N(t)} \rho_p$ and $u_{MD} = \sum\limits_{p=1,N(t)} u_{ip}\rho_p / \rho_{MD}$, plotted as a function of radial distance in the hybrid part of the simulation domain where *s* varies from 0 to 1. The vertical dotted lines represent the boundaries of the hybrid zone and the theoretical solution values are denoted with subscript 0. It can be seen that the density is preserved within 0.1% and the momentum is preserved within 0.5% of the mean density and the product of the mean density

32

and the speed of sound, respectively. The latter way of normalisation for momentum was chosen since the meanflow velocity is zero.
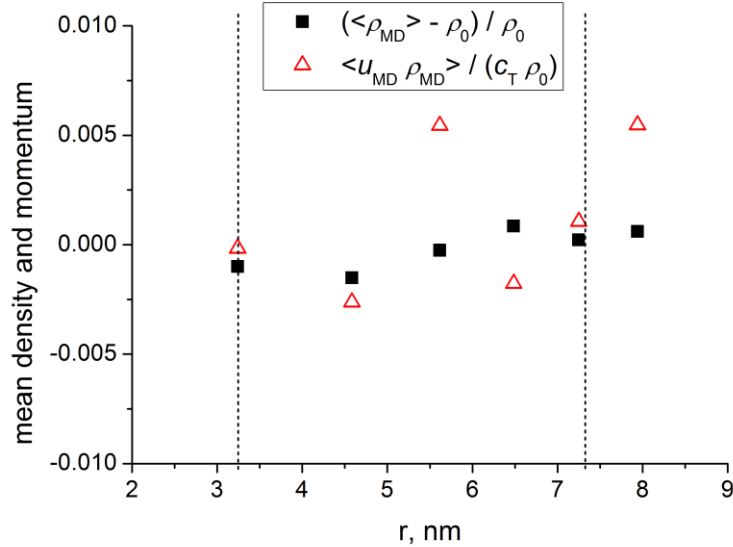

**Figure 14.** Variation of time averaged density and momentum across the hybrid zone $0 < s < 1$ shown by the vertical dotted lines (left, $s = 0$ and right, $s = 1$) for argon.

The standard deviations of density and velocity of the MD part of the hybrid solution across the hybrid zone fluctuates 5-7% around the theoretical values. The results are obtained for argon and remain similar for the case of the water model considered in the next section.
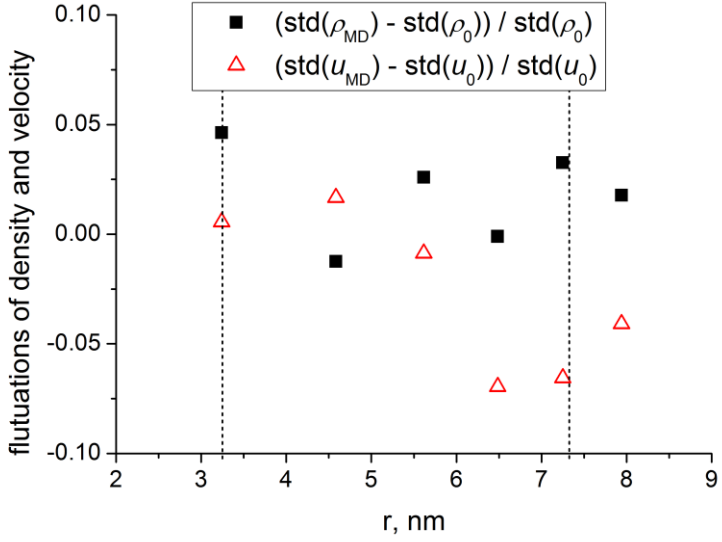
Figure 15. Variation of standard deviation of density and momentum across the hybrid zone $0 < s < 1$ shown by the vertical dotted lines (left, $s = 0$ and right, $s = 1$) for argon.

To confirm that the MD part of the solution satisfies to the Fluctuation Dissipation Theorem, one needs to show that (i) the auto-correlation amplitudes of density and velocity are correct and (ii) the density and velocity fluctuations are uncorrelated, e.g. the autocorrelations of both are close to delta function within the noise level. The preservation of correct fluctuations across the hybrid MD/FH zone has been demonstrated in Fig.15. Figs. 16a,b shows the corresponding autocorrelations of the density and x-velocity component fluctuations of the MD part of the solution, respectively, where the reference location x_0 is taken at the middle of the MD/FH hybrid zone which correspond to $s = 0.5$. Both autocorrelation functions abruptly decay for non-zero spatial separations $|\delta_x| > 0$. The noisy background of the autocorrelation functions is likely to be associated with insufficient temporal averaging. Note that there was no spatial averaging to

compensate for the lack of the temporal statistics convergence attempted to cosmetically reduce the noise.
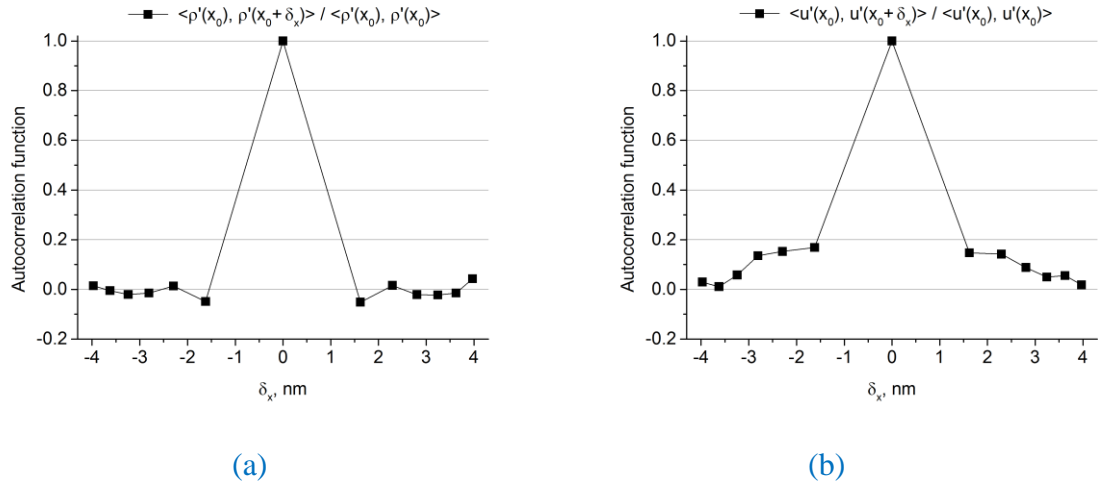

Figure 16. Autocorrelations of (a) density and (b) *x*-velocity component for argon for the location x_0 at the centre of the hybrid MD/LL-FH zone.

To conclude this section, the present hybrid method is probed for its ability to correctly transport acoustic wave through the MD/LL-FH zone. The acoustic wave propagation test is essentially to show how well the hybrid scheme conserves the momentum in unsteady flow.

For the test, the solution domain consisting of 20 x 5 x 5 cells (x times y times z) is selected which in total contains 32000 argon atoms with a 'pure' MD zone in the centre in between the two LL-FH zones at the inlet and outlet. A periodic acoustic wave solution is specified as the inlet boundary condition of the solution domain so that its wavelength is exactly equal to the length of the solution domain in the x-direction and periodic boundary conditions for particles still hold. The acoustic wave boundary condition was implemented through adding the analytical source terms in the governing LL-FH equations in the inlet boundary cells. The source terms correspond to the time derivatives of density and velocity of the incoming acoustic wave of a

small amplitude propagating over the prescribed constant meanflow field of the LL-FH solution. The density fluctuation signal is computed in the 'probe' point located in the centre of the 'pure' MD region and compared with the analytical solution.

Fig.17a compares the fluctuating density signal with the analytical solution. Due to a very low acoustic signal to thermal noise ratio (~0.01), the original signal is completely masked by the presence of thermal density fluctuations. However, in accordance with the Fluctuation Dissipation Theorem, the thermal density fluctuations are uncorrelated, and after the phase averaging as well as the additional spatial averaging in the normal plane to the acoustic wave propagation (*y-z*), the fluctuating density signal of the MD solution becomes very close to the analytical solution specified (fig.17b). Notably, the discrepancy between the computed density fluctuation in the MD zone after the averaging and the analytical solution is of the same order of magnitude as the noise level in the same hybrid model without the acoustic wave.
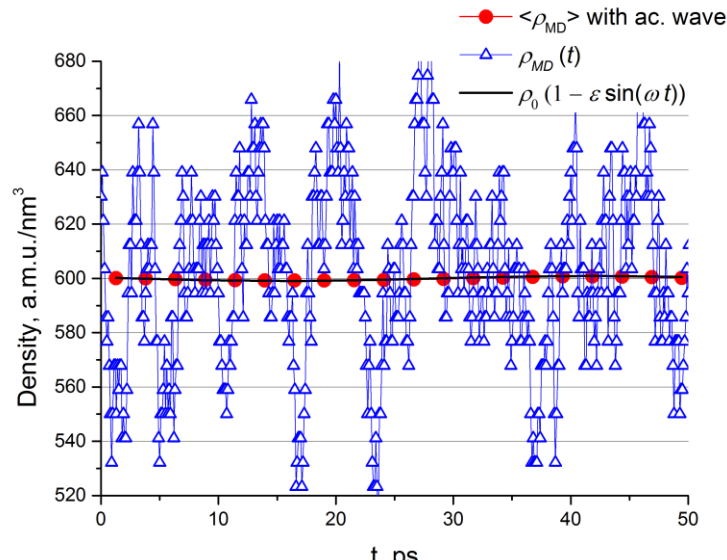
(a)
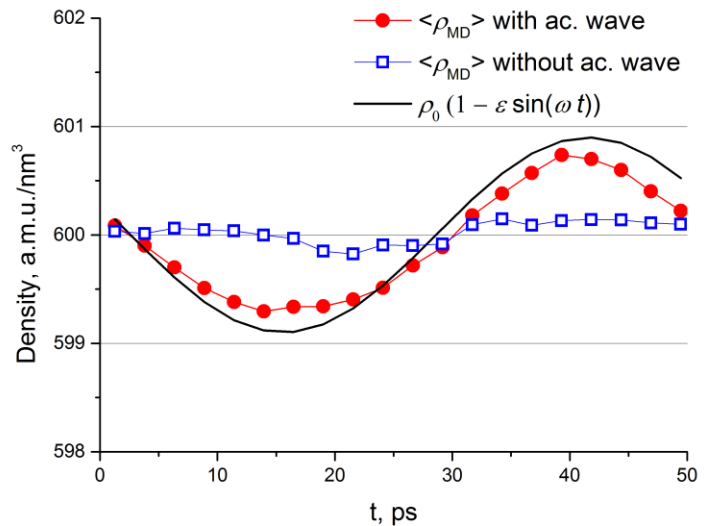
(b)

Figure 17. Fluctuating density signal obtained in the MD part of the solution domain vs the analytical solution (a) including the original MD signal without phase and space averaging, (b) zoomed-in view with including the reference phase and space averaged solution without the acoustic wave.

3.3 Dialanine in water

The next step is to add a small peptide molecule, the zwitterionic form of dialanine, into water. A single peptide molecule is initially placed in the centre of the MD sphere (the $s = 0$ region depicted in Fig. 1) and surrounded by our hybrid SPC-E/hydrodynamic water model. The initial configuration is depicted in Fig 18.
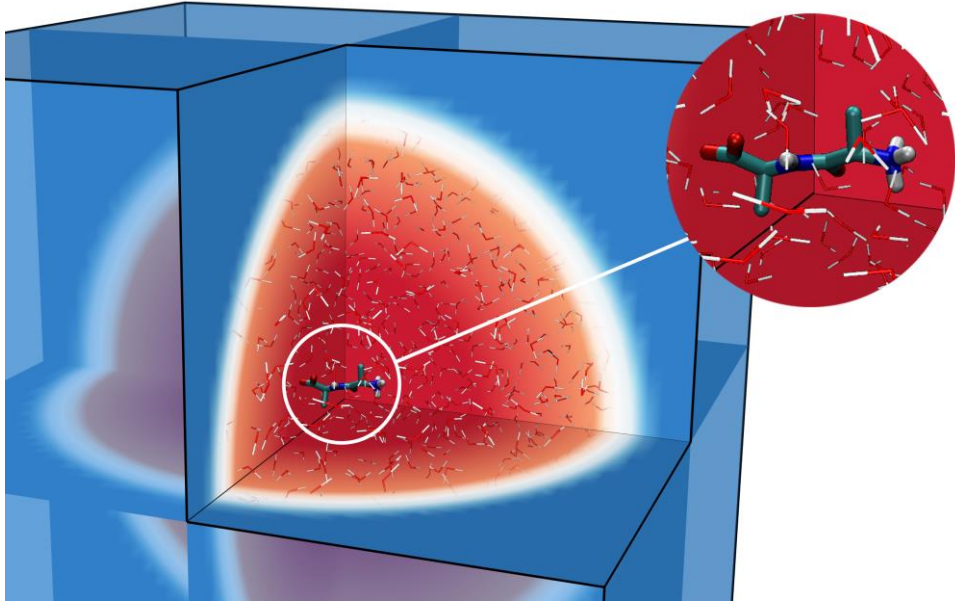
Figure 18. Variable *s* parameter and MD sphere inside the computation box with a small peptide molecule, the zwitterionic form of dialanine, at the centre of the sphere. The red sphere is the pure MD region ($s = 0$), blue is the fluctuating hydrodynamics region ($s=1$).

The simulation is stopped when the macromolecule reaches the hybrid MD/LL-FH zone, which is currently fixed in space in accordance with (14). To prolong the simulation time, in our future work, a non-stationary MD zone will be considered by linking (14) to the movement of the centre of mass of the peptide system so that the coupling parameter in (9) becomes a function of space and time, $s = s(x, y, z, t)$.

To check the influence of the hydrodynamics dominated region ($s > 0$) on the MD region ($s = 0$) we have calculated the translational self-diffusion coefficients D for both water and peptide molecules in this region and compared them with the ones obtained from a pure MD simulation. The Einstein relation was used for calculating D: $MSD(t) = \left\langle \Delta r(t)^2 \right\rangle = A + 6Dt$, where A is an arbitrary constant. Importantly, this formula is correct only at long times (it is exact in the infinitely long times). In practice, the part of the curve that can be satisfactory

approximated by a straight line should be taken in the account. In other words, it is the local slope of the MSD trajectory at long times which should be considered and the initial fluctuations of MSD at short times should be discarded when calculating D.

All simulations (pure and hybrid) have been carried out at the same conditions: $T = 298$ K (Nose-Hoover thermostat); constant density $\rho = 999.15$ g/cm^3 for water and 992.92 g/cm^3 for peptide solution; the MD time step $\Delta t = 1$ fs; the reaction field electrostatics with cut-off length 0.9 nm and dielectric constant 78; van der Waals cut-off 0.9 nm.

When evaluating D in the pure MD simulations a 10 ns long simulation of water and 40 ns long simulation of the peptide solution were performed. The MSD(t) plots were calculated for 1 ns intervals and then averaged (Fig. 19). The obtained values of D are: D(water) = 2.68·10^{-5} cm^2/s, D(protein) = 0.86·10^{-5} cm^2/s.
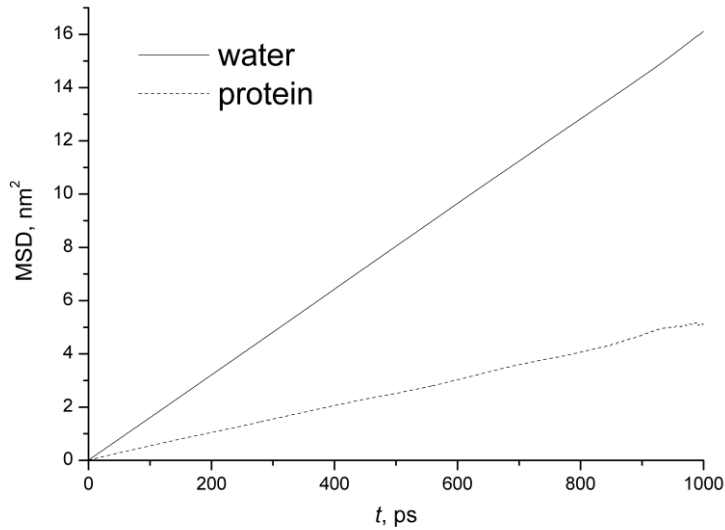

Figure 19. The MSD(t) plot for the SPC/E water and the protein from a pure MD simulation

However, evaluating D in the hybrid multiscale model case is not straightforward because, unlike the single-scale MD, the test molecule leaves the inner MD sphere beyond which the hydrodynamics dominated region starts where the individual molecule diffusion is not represented correctly. Therefore, special measures have been taken to correctly calculate the MSD. The former are not dissimilar to special measures that need to be taken for the verification of other multiscale algorithms that undergo several scales in comparison with a single scale problem [64].

As it takes a relatively short time for the molecule to reach the hybrid zone, there is no reason to carry out long simulations, and the typical algorithm, similar to the mentioned above, becomes inappropriate. Therefore, we proceeded by obtaining many short single molecule MSD(t) plots and averaging them to accumulate a statistically sound data. On the one hand long trajectories are needed to satisfy the long time limit condition of the Einstein relation, on the other hand the longer simulations are, the less molecules remain in the $s = 0$ region. Therefore, it is necessary to: (i) have the molecules of interest in the centres of their boxes at the beginning of the simulation and (ii) to exclude the molecules that visited the region $s > 0$ from averaging the MSD(t) plots.

To satisfy these requirements we used the following algorithm:

1. *Preparing the initial cells*. During the initial equilibration the peptide molecule was fixed at the box centre by applying restrains to the peptide bond carbon. In total 70 cells with water and 182 cells with peptide solution were prepared starting from different initial configurations.

2. *Collecting data*. Hybrid MD runs were 200 ps length. Starting from 80 ps, every 20 ps frame was extracted for further analysis. The MSD(t) plot was calculated for each trajectory. In

each pure water simulation, those molecules that were already situated in the centre of the initial cell were used (1–5 molecules per cell).

3. *Filtering*. By analysing the extracted frames, the trajectories with the test molecules that visited the $s > 0$ region were identified and excluded from the sampling set. The filtration criterion was the distance between the geometrical centre of the molecules and the cell centre. These should be less than a cut-off radius R_c. We investigated several cut-off radii R_c ranging from 1.3 to 2.9 nm.

4. *Evaluating D*. The obtained MSD(t) plots, Fig. 20 an Fig. 21, were averaged over the single molecule MSD(t) plots obtained after filtering. Both water and peptide MSD(t) plots are almost the same below some value of R_c (2.1 nm for water and 1.5 nm for peptide) which suggests that results are reasonably independent of R_c and further reducing of the cut-off R_c is not needed. The fitting for D was done at the intervals in the middle of the plots (40–80 ps for water and 45–70 ns for peptide solution). The part at small times does not satisfy the Einstein relation requirement, while the ending parts are affected by the closeness of the hybrid zone. The final D is calculated as the average over the three smallest cut-off radii R_c (Tables 2 and 3).
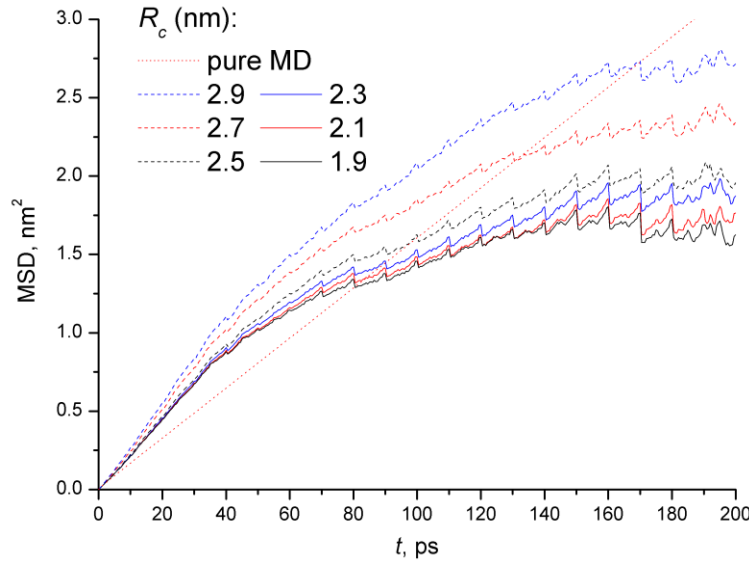
Figure 20. The MSD(t) plots for water (hybrid MD) calculated with different cut-off radii. The

pure MD plot is given for comparison
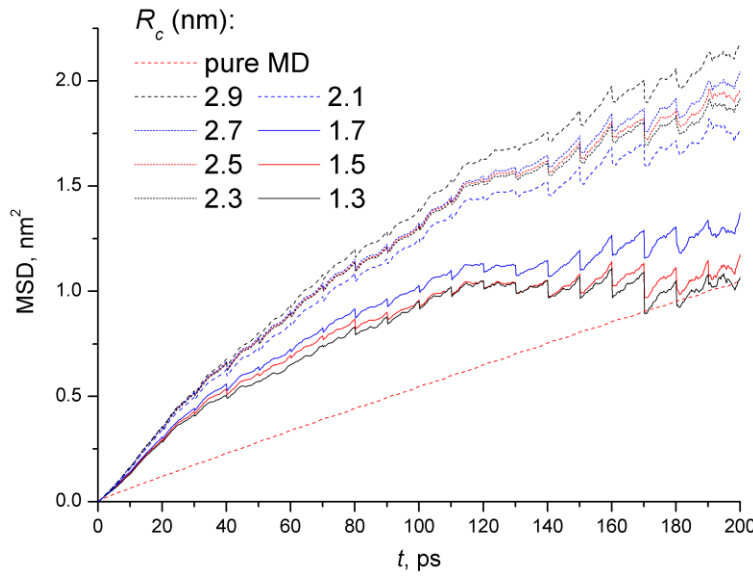
Figures 21. The MSD(t) plots for protein (hybrid MD) calculated with different cut-off radii.

The Pure MD plot is given for comparison

Table 2. The diffusion coefficient D obtained in hybrid simulations.

R_c, nm	D, 10^{-5} cm^2/s
water	
2.3	2.25
2.1	2.15
1.9	2.01
protein	
1.7	1.53
1.5	1.42
1.3	1.37

Table 3. Final D values (the errors for the pure MD results are negligibly small)

	D, 10^{-5} cm^2/s	
	pure MD	Hybrid
Water	2.68	2.1 ± 0.12
Peptide	0.86	1.4 ± 0.16

The uncertainty of D was estimated as the sum of two errors, which were assumed to be uncorrelated:

1) In the whole fitting interval the 20 ps (protein) or 15 ps (water) sections were extracted with the 10 ps shift. Several D_i values were calculated from this sections by fitting, and the half of the range between the smallest and the biggest D_i was taken as a slope uncertainty ΔDsl.

2) The dependence on R_c was accounted with cut-off uncertainty ΔD_c, given by:

$$\Delta D_c = \left| \frac{\partial D}{\partial R_c} \right| \Delta R_c \approx \left| \frac{D(R_{c2}) - D(R_{c1})}{R_{c2} - R_{c1}} \right| \Delta R_c ,$$

where ΔR_c was taken to be 0.2 nm, so that the total uncertainty is given by

$$\Delta D = \sqrt{\Delta Dsl^2 + \Delta D_c^2} .$$

The final diffusion coefficients D are listed in Table 3. Our hybrid method somewhat overestimates D for water molecules and underestimates it for the peptide. With taking into account the uncertainties, the discrepancy between the hybrid model and the reference MD

simulation is about 20% for water and 30% for peptide, respectively. We attribute this to the smallness of the MD zone where test molecules are monitored and its closeness to the hybrid zone. The first effect reduces the statistical sampling available for post-processing to determine such a nonlocal quantity as the molecular diffusion coefficient, while the second generates artefact interactions between the test molecules in the MD zone and the hydrodynamics dominated zone, as discussed in section 3.1. To alleviate these effects, a bigger MD zone and a thicker hybrid zone will be implemented in our future work.

1. Conclusion and discussion

The following has been demonstrated:

(i) for constant *s*-parameter, the current 3D implementation of the hybrid method correctly captures the macroscopic fluctuations of density and velocity in accordance with the literature;

(ii) for variable *s*-parameter, despite some sensitivity to the size of the hybrid MD/LL-FH zone noted, the hybrid method preserves important structure functions of liquids such as the radial distribution function as well as the velocity autocorrelation function in the atomistic part of the solution; the change of the structure functions is gradual under the effect of coarse graining when the influence of hydrodynamics on MD is introduced;

(iii) it has been shown that the mass and momentum of the MD part of the solution are preserved in the hybrid MD/LL-FH zone within 0.5%;

(iv) the autocorrelations of density and velocity of the MD part of the solution are correctly preserved in the hybrid MD/LL-FH zone in accordance with the Fluctuation Dissipation Theorem;

(v) the results of the travelling acoustic wave through the hybrid MD/LL-FH region have demonstrated the capability of the method to correctly transfer the momentum in unsteady flow within the accuracy of statistical noise;

(vi) preliminary results of the hybrid method for water molecular diffusion and the dialanine diffusion in water show a reasonable agreement with the reference MD simulation.

Further work will be devoted to implementing a larger simulation box to reduce the sensitivity of the solution to the size of the hybrid MD/LL-FH region. For example, this might be achieved by introduction of gradually expanding space-time scales into the simulation in order to obtain a more gradual transition from the small atomistic scales to the large hydrodynamic scales. The expansion of space-time scales in the hybrid zone, from atomistic to hydrodynamic scales where the MD particle would lose their mobility because of small thermal fluctuations in large cell volumes, is also expected to constrain the location of the MD particles mainly to the atomistic part of the solution domain. Constraining MD particles to a small fraction of the hydrodynamic solution domain is essential to further increase the computational benefits of the hybrid method in comparison with the all-atom simulation. Currently, the efficiency of the present model implementation, which employs MD particles everywhere including the hydrodynamics dominated zone, in comparison with the all-atom simulation is just due to not computing the molecular potentials in the hydrodynamics dominated part of the solution domain. Additionally, the 3D implementation of the two-way coupling scheme, including the feedback from atomistic scales to hydrodynamics, as well as including the energy conservation equation into the coupling framework, which would be essential for nonzero flows such as shear and non-isothermal processes, remain our further lines of work.

2. Acknowledgements

3. References

1. W. Young, H. David, and R. Talreja, eds., Multiscale Modeling and Simulation of Composite Materials and Structures, 6th ed. (Springer, Chichester, 2007)

2. D. Vlachos, Advances in Chemical Engineering 30, 1 (2005)

3. D. Nerukh and S. Karabasov, J. Phys. Chem. Lett. 4, 815 (2013)

4. H. Frauenfelder, G. Chen, J. Berendzen, P.W. Fenimore, H. Jansson, B. H. McMahon, I.R. Stroe, J. Swenson, and R.D. Young, Proc. Natl. Acad. Sci. USA 106, 5129 (2009)

5. B. West, F. Brown, and F. Schmid, Biophy. J. 96, 101 (2009)

6. R. Lonsdale, S. Rouse, M. Sansom, and A. Mulholland, PLOS Computational Biology 10, 1 (July 2014)

7. P.M. Kasson and V.S. Pande, Paci_c Symposium on Biocomputing 15, 260 (2010)

8. D.S.D. Larsson, L. Liljas, D. van der Spoel (2012), PLoS Comput Biol 8(5): e1002502. doi:10.1371/journal.pcbi.1002502

9. M. Zink, H. Grubmüller. Biophysical Journal. Volume 98, Issue 4, Pages 687-695 (February 2010). DOI: 10.1016/j.bpj.2009.10

10. E.G. Flekkoy, G. Wagner, and J. Feder, Eur Lett 52, 271 (2000)

11. A. Asproulis, M. Kalweit, and D. Drikakis, Advances in Engineering Software 46, 85 (2012)

12. A. Markesteijn, S. Karabasov, A. Scukins, D. Nerukh, V. Glotov and V. Goloviznin, Phil. Trans. R. Soc. A 2014 372, 20130379

13. S.O. Connel and P. Thompson, Phys. Rev E. 52, 5792 (1995)

14. E. Kotsalis, J. Walther, and P. Koumoutsakos, Physical Review E 76, 016709 (2007)

15. E. Kotsalis, J. Walther, E. Kaxiras, and P. Koumoutsakos, Physical Review E 79 (2009)

16. G. Fabritiis, R. Delgado-Buscalioni, and P.V. Coveney, Physical Review Letters 97, 134501 (2006)

17. E. W. Nie X., Chen E. and M. O. Robbins, J. Fluid Mech. 500, 55 (2004)

18. E. Pavlov, M. Taiji, A. Scukins, A. Markesteijn, S. Karabasov, and D. Nerukh, Faraday Discuss., 2014,169, 285-302, DOI: 10.1039/C3FD00159H

19. N. Pasquale, D. Marchisio, and P. Carbone, Journal of Chemical Physics 137, 164111 (2012)

20. W.G. Noid, J. Chu, S.G. Ayton, V. Krishna, S. Izvekov, G. A. Voth, A. Das, and H. Andersen, J. Chem. Phys. 128, 244114 (2008)

21. F. Muller-Plathe, Chem Phys Chem 3, 755 (2002)

22. Y. Tang and G. Karniadakis, CoRR (2013)

23. P. J. Hoogerbrugge and A. Koelman, Europhysics Letters 19(3), 155 (2014)

24. P. Espanol, Europhysics Letter 40, 631 (1997)

25. H. Wu, J. Xu, S. Zhang, and H. Wen, IEIT Journal of Adaptive and Dynamic Computing 1, 33 (2011)

26. H. J. C. Berendsen, et al. (1995) *Comp. Phys. Comm.* **91:** 43-56

27. N. Goga, S. Costashe, and S. Marrik, MATERIALE PLASTICE , 53 (2009)

28. N. Goga, S. Marrink, and S. Costache, 3rd Annual IEEE International Systems Conference (2009)

29. S.J. Marrink et al., J Phys.Chem B 111(27), 7812 (2007)

30. F. Buti, D. Cacciagrano, F. Corradini, E. Merelli, and L. Tesei, Procedia Computer Science 00, 19 (2010)

31. W. G. Noid, J-W Chu, G. S. Ayton, and G. A. Voth, J. Phys. Chem. B (2007), 111, 4116-4127

32. M. Praprotnik, L. Delle Site, and K. Kremer, J. Chem. Phys. 126, 134902 (2007), doi: 10.1063/1.2714540

33. R. Potestio, S. Fritsch, P. Español, R. Delgado-Buscalioni, K. Kremer, R. Everaers and D. Donadio, PRL 110, 108301 (2013), doi: 10.1103/PhysRevLett.110.108301

34. P. Español, R. Delgado-Buscalioni, R. Everaers, R. Potestio, D. Donadio, and K. Kremer, J. Chem. Phys. 142, 064115 (2015), doi: 10.1063/1.4907006

35. G. De Fabritiis, R. Delgado-Buscalioni, P.V. Coveney. 2006, Phys. Rev. Lett. 97, 134501. (doi:10.1103/PhysRevLett.97 134501)

36. M.J. Lighthill, Proc. Royal Soc. of London A, (1952), 222, 564-587

37. M.E. Goldstein, J. Fluid Mech., (2003), 488, 315-333

38. M.E. Goldstein and S. J. Leib, J. Fluid Mech., (2008), 600, pp.291-337

39. S. A. Karabasov, Phil. Trans. R. Soc. A, (2010), vol. 368, 3593-3608

40. S.E. Buckley, M.C. Leverett, *Trans. AIME* **146**, 107–116 (1942)

41. A. Scukins, D. Nerukh, E. Pavlov, S. Karabasov, and A. Markesteijn, EPJ ST, (2015)

42. A. Ben-Naim, J. Chem. Phys., vol. 54, p. 3682, (1971)

43. L.D. Landau, E.M. Lifshitz, 1980 Statistical physics part 1. Amsterdam, The Netherlands: Elsevier

44. J. M. Ortiz de Zárate, J. V. Sengers, 2006, "Hydrodynamic Fluctuations in Fluids and Fluid Mixtures", Amsterdam, The Netherlands: Elsevier

45. J.B. Bell, A.L. Garcia, S.A.Williams, Phys. Rev. E76 (2007)

46. A. Donev, E. Vanden-Eijnden, A.L. Garcia, J. B. Bell, Commun. Appl. Math. Comput. Sci. 5 (2) (2010)

47. A.P. Markesteijn, S.A. Karabasov, V.Yu. Glotov, V.M. Golovznin, Comput. Methods Appl. Mech. Engrg. 281 (2014) 29–53

48. G. De Fabritiis, M. Serrano, R. Delgado-Buscalioni, P.V. Coveney. 2007, Phys. Rev. E 75, 026307. (doi:10.1103/PhysRevE.75.026307)

49. N.K. Voulgarakis, J-W. Chu, 2009, J. Chem. Phys. 130, 134111. (doi:10.1063/1.3106717)

50. J.C. Ladd, Phys. Rev. Lett. 70, 1339–1342, (1993). (doi:10.1103/PhysRevLett.70. 1339)

51. A.P. Markesteijn, O.B. Usta, I. Ali, A.C. Balazs, J.M. Yeomans, Soft Matter 5 (2009) 4575-4579

52. F.B Usabiaga, J. Bell, R. Delgado-Buscalioni, A. Donev, T. Fai, B. Griffith, and C. Peskin, Multiscale Modeling and Simulation, 10, 4, 1360-1408, 2012

53. J.H. Irving and J.G. Kirkwood, J. Chem. Phys. 18, 817 (1950)

54. A.P. Markesteijn, R. Hartkamp, S. Luding, and J. Westerweel, J. Chem. Phys. 136, 134104 (2012)

55. A.P Sunda, and A Venkatnathan, Molecular Simulation, Volume 39, Issue 9, 2013, pages 728-733, DOI:10.1080/08927022.2012.762098

56. G-J Guo and Y-G Zhang, Molecular Physics: An International Journal at the Interface Between Chemistry and Physics, Volume 99, Issue 4, 2001, pages 283-289, DOI:10.1080/00268970010011762

57. G.S. Fanourgakis, J.S. Medina, and R. Prosmiti, J. Phys. Chem. A, 2012, 116 (10), pp 2564–2570, DOI: 10.1021/jp211952y

58. M.A. González and J.L.F. Abascal, J. Chem. Phys. 132, 096101 (2010); http://dx.doi.org/10.1063/1.3330544

59. B. Z. Shang, N.K. Voulgarakis, and J-W Chua, J. Chem. Phys. 137, 044117 (2012)

60. S.A. Nosé, Mol. Phys. 52:255–268, 1984

61. W.G. Hoover, Phys. Rev. A 31:1695–1697, 1985

62. H. J. C. Berendsen, J. G. E. M. Fraaije, Journal of Computational Chemistry 18 (12): 1463–1472 (1997)

63. A.P. Markesteijn and S.A. Karabasov, J. Comp. Phys., 258, 137-164 (2014)

64. S. Karabasov, D. Nerukh, A. Hoekstra, B. Chopard, and P.V. Coveney, Phil. Trans. R. Soc. A 2014 372, 20130390 (2014)

Appendix A

Substituting the expressions for $\frac{d\mathbf{x}_p}{dt}$ and $\frac{du_{ip}}{dt}$ from (9) to (8) yields:

$$\delta_t\left(\sum_{p=1,N(t)} m_p\right)+\sum_{\gamma=1,6}\left(\sum_{p=1,N_\gamma(t)}\mathbf{u}_p\rho_p\right)d\mathbf{n}^\gamma\cdot\delta t=-\sum_{\gamma=1,6}\left(\sum_{p=1,N_\gamma(t)}s(\bar{\mathbf{u}}-\mathbf{u}_p)\rho_p\right)d\mathbf{n}^\gamma\cdot\delta t$$

$$-\sum_{\lambda=1,6}\left(s(1-s)\cdot\alpha\cdot\frac{1}{V}\sum_{\gamma=1,6}\left(\bar{\rho}-\sum_{q=1,N_\gamma(t)}\rho_q\right)d\mathbf{n}^\gamma\right)d\mathbf{n}^\lambda\cdot\delta t$$

(A1)

and

$$\delta_t\left(\sum_{p=1,N(t)} m_p u_{ip}\right)+\sum_{\gamma=1,6}\left(\sum_{p=1,N_\gamma(t)}\mathbf{u}_p\rho_p u_{ip}\right)d\mathbf{n}^\gamma\cdot\delta t=\sum_{p=1,N(t)}(1-s)F_{ip}\cdot\delta t$$

$$+\sum_{k=1,3}\sum_{\gamma=1,6}\left(s(1-s)\beta\frac{1}{V}\sum_{\lambda=1,6}\left(\bar{\rho}\cdot\bar{u}_i-\sum_{q=1,N_\lambda(t)}\rho_q u_{iq}\right)dn_k^\lambda\right)dn_k^\gamma\,\delta t-\sum_{\gamma=1,6}\left(\sum_{p=1,N_\gamma(t)}s(\bar{\mathbf{u}}-\mathbf{u}_p)\rho_p u_{ip}\right)d\mathbf{n}^\gamma\delta t,$$

(A2)

respectively.

By subtracting the following true identities for density and momentum from equations (A1) and (A2), respectively,

$$\delta_t\left(s\sum_{p=1,N(t)} m_p\right)+\sum_{\gamma=1,6}s\left(\sum_{p=1,N_\gamma(t)}\mathbf{u}_p\rho_p\right)d\mathbf{n}^\gamma\delta t=\delta_t\left(s\sum_{p=1,N(t)} m_p\right)+\sum_{\gamma=1,6}s\left(\sum_{p=1,N_\gamma(t)}\mathbf{u}_p\rho_p\right)d\mathbf{n}^\gamma\delta t$$ (A3)

and

$$\delta_t\left(s\sum_{p=1,N(t)} m_p u_{ip}\right)+\sum_{\gamma=1,6}s\left(\sum_{p=1,N_\gamma(t)}\mathbf{u}_p\rho_p u_{ip}\right)d\mathbf{n}^\gamma\delta t=$$

$$=\delta_t\left(s\sum_{p=1,N(t)} m_p u_{ip}\right)+\sum_{\gamma=1,6}s\left(\sum_{p=1,N_\gamma(t)}\mathbf{u}_p\rho_p u_{ip}\right)d\mathbf{n}^\gamma\delta t,$$

(A4)

the following equations are obtained:

$$\delta_t\left((1-s)\sum_{p=1,N(t)}m_p\right)+\sum_{\gamma=1,6}(1-s)\left(\sum_{p=1,N_\gamma(t)}\mathbf{u}_p\rho_p\right)d\mathbf{n}^\gamma\delta t=-\delta_t\left(s\sum_{p=1,N(t)}m_p\right)-$$

$$-\sum_{\gamma=1,6}\left(\sum_{p=1,N_\gamma(t)}s\bar{\mathbf{u}}\rho_p\right)d\mathbf{n}^\gamma\delta t-\sum_{\lambda=1,6}\left(s(1-s)\cdot\alpha\cdot\frac{1}{V}\sum_{\gamma=1,6}\left(\bar{\rho}-\sum_{q=1,N_\gamma(t)}\rho_q\right)d\mathbf{n}^\gamma\right)d\mathbf{n}^\lambda\delta t$$

(A5)

and

$$\delta_t\left((1-s)\sum_{p=1,N(t)}m_pu_{ip}\right)+\sum_{\gamma=1,6}(1-s)\left(\sum_{p=1,N_\gamma(t)}\mathbf{u}_p\rho_pu_{ip}\right)d\mathbf{n}^\gamma\delta t-\sum_{p=1,N(t)}(1-s)F_{ip}\,\delta t=$$

$$-\delta_t\left(s\sum_{p=1,N(t)}m_pu_{ip}\right)-\sum_{\gamma=1,6}\left(\sum_{p=1,N_\gamma(t)}s\bar{\mathbf{u}}\rho_pu_{ip}\right)d\mathbf{n}^\gamma\delta t+$$

$$+\sum_{k=1,3}\sum_{\gamma=1,6}\left(s(1-s)\cdot\beta\cdot\frac{1}{V}\sum_{\lambda=1,6}\left(\bar{\rho}\cdot\bar{u}_i-\sum_{q=1,N_\gamma(t)}\rho_qu_{iq}\right)dn_k^\lambda\right)dn_k^\gamma\,\delta t$$

(A6)

Comparison of (A5) and (A6) with (2) and (4), respectively, gives:

$$\delta_tJ^{(\rho)}=\delta_t\left(s\sum_{p=1,N(t)}m_p\right)+\sum_{\gamma=1,6}\left(\sum_{p=1,N_\gamma(t)}s\bar{\mathbf{u}}\rho_p\right)d\mathbf{n}^\gamma\cdot\delta t+$$

$$+\sum_{\lambda=1,6}\left(s(1-s)\cdot\alpha\cdot\frac{1}{V}\sum_{\gamma=1,6}\left(\bar{\rho}-\sum_{q=1,N_\gamma(t)}\rho_q\right)d\mathbf{n}^\gamma\right)d\mathbf{n}^\lambda\delta t$$

(A7)

and

$$\delta_tJ_i^{(\mathbf{u})}=\delta_t\left(s\sum_{p=1,N(t)}m_pu_{ip}\right)+\sum_{\gamma=1,6}\left(\sum_{p=1,N_\gamma(t)}s\bar{\mathbf{u}}\rho_pu_{ip}\right)d\mathbf{n}^\gamma\delta t-$$

$$-\sum_{k=1,3}\sum_{\gamma=1,6}\left(s(1-s)\cdot\beta\cdot\frac{1}{V}\sum_{\lambda=1,6}\left(\bar{\rho}\cdot\bar{u}_i-\sum_{q=1,N_\gamma(t)}\rho_qu_{iq}\right)dn_k^\lambda\right)dn_k^\gamma\,\delta t.$$

(A8)

By substituting the above expressions (A7) and (A8) into the continuum 'phase' equations (1) and (3), summing up the results for the mass

$$\delta_t(sm) + \sum_{\gamma=1,6}\left(s\rho\bar{\mathbf{u}}\right)d\mathbf{n}^\gamma\delta t = \delta_t\left(s\sum_{p=1,N(t)}m_p\right) + \sum_{\gamma=1,6}\left(\sum_{p=1,N_\gamma(t)}s\bar{\mathbf{u}}\rho_p\right)d\mathbf{n}^\gamma\delta t +$$

$$+\sum_{\lambda=1,6}\left(s(1-s)\cdot\alpha\cdot\frac{1}{V}\sum_{\gamma=1,6}\left(\bar{\rho} - \sum_{q=1,N_\gamma(t)}\rho_q\right)d\mathbf{n}^\gamma\right)d\mathbf{n}^\lambda\delta t \qquad (A9)$$

and momentum,

$$\delta_t(smu_i) + \sum_{\gamma=1,6}\left(s\rho u_i\bar{\mathbf{u}}\right)d\mathbf{n}^\gamma\delta t = \delta_t\left(s\sum_{p=1,N(t)}m_p u_{ip}\right) + \sum_{\gamma=1,6}\left(\sum_{p=1,N_\gamma(t)}s\bar{\mathbf{u}}\rho_p u_{ip}\right)d\mathbf{n}^\gamma\delta t +$$

$$+s\sum_{j=1,3}\sum_{\gamma=1,6}\left(\Pi_{ij}+\tilde{\Pi}_{ij}\right)dn_j^\gamma\,\delta t - \qquad (A10)$$

$$-\sum_{k=1,3}\sum_{\gamma=1,6}\left(s(1-s)\cdot\beta\cdot\frac{1}{V}\sum_{\lambda=1,6}\left(\bar{\rho}\cdot\bar{u}_i - \sum_{q=1,N_\gamma(t)}\rho_q u_{iq}\right)dn_k^\lambda\right)dn_k^\gamma\,\delta t$$

with the following true identities

$$\delta_t\left((1-s)\sum_{p=1,N(t)}m_p\right) + \sum_{\gamma=1,6}(1-s)\left(\sum_{p=1,N_\gamma(t)}\bar{\mathbf{u}}\rho_p\right)d\mathbf{n}^\gamma\delta t =$$

$$= \delta_t\left((1-s)\sum_{p=1,N(t)}m_p\right) + \sum_{\gamma=1,6}(1-s)\left(\sum_{p=1,N_\gamma(t)}\bar{\mathbf{u}}\rho_p\right)d\mathbf{n}^\gamma\delta t \qquad (A11)$$

and

$$\delta_t\left((1-s)\sum_{p=1,N(t)}m_p u_{ip}\right) + \sum_{\gamma=1,6}(1-s)\left(\sum_{p=1,N_\lambda(t)}s\bar{\mathbf{u}}\rho_p u_{ip}\right)d\mathbf{n}^\gamma\delta t =$$

$$= \delta_t\left((1-s)\sum_{p=1,N(t)}m_p u_{ip}\right) + \sum_{\gamma=1,6}(1-s)\left(\sum_{p=1,N_\gamma(t)}s\bar{\mathbf{u}}\rho_p u_{ip}\right)d\mathbf{n}^\gamma\delta t \qquad (A12)$$

respectively, and using the mixture density and momentum variables, $\bar{\rho} = s\rho + (1-s)\sum_{p=1,N(t)}\rho_p$

and $\overline{m}\bar{u}_i = smu_i + (1-s)\sum_{p=1,N(t)}m_p u_{ip}$, respectively, finally yields:

$$\delta_t \left(\bar{m} - \sum_{p=1,N(t)} m_p \right) + \sum_{\gamma=1,6} \bar{\mathbf{u}} \left(\bar{\rho} - \sum_{q=1,N_\gamma(t)} \rho_q \right) d\mathbf{n}^\gamma \delta t =$$

$$-\sum_{\lambda=1,6} \left(s(1-s) \cdot \alpha \cdot \frac{1}{V} \sum_{\gamma=1,6} \left(\bar{\rho} - \sum_{q=1,N_\gamma(t)} \rho_q \right) d\mathbf{n}^\gamma \right) d\mathbf{n}^\lambda \delta t$$

(A13)

and

$$\delta_t (\bar{m} \cdot \bar{u}_i - \sum_{p=1,N(t)} m_p u_{ip}) + \sum_{\gamma=1,6} s\bar{\mathbf{u}} \left(\bar{\rho} \cdot \bar{u}_i - \sum_{p=1,N_\gamma(t)} \rho_p u_{ip} \right) d\mathbf{n}^\gamma \delta t =$$

$$= s \sum_{j=1,3} \sum_{\gamma=1,6} \left(\Pi_{ij} + \tilde{\Pi}_{ij} \right) dn_j^\gamma \, \delta t -$$

(A14)

$$-\sum_{k=1,3} \sum_{\gamma=1,6} \left(s(1-s) \cdot \beta \cdot \frac{1}{V} \sum_{\lambda=1,6} \left(\bar{\rho} \cdot \bar{u}_i - \sum_{q=1,N_\lambda(t)} \rho_q u_{iq} \right) dn_k^\lambda \right) dn_k^\gamma \, \delta t.$$

The resulting equations (A13) and (A14) are identical to (5)-(7).